# Tissue-scale mechanics controls differentiation strategy and dynamics of epithelial multilayering

Clémentine Villeneuve[1, 2]*, Somiealo Azote Epse Hassikpezi [3]*, Marga Albu[2], Matthias Rübsam[4], Leah C. Biggs[1,2], Sabrina Vinzens[2], Kai Kruse[5], Anubhav Prakash[2], Peter Zentis[6], Elizabeth Lawson-Keister[3], Gautier Follain[7,8,9], Johanna Ivaska[7,10,11], Carien M. Niessen[4§], M. Lisa Manning[3§], and Sara A. Wickström[1,2,12§]

[1]Stem Cells and Metabolism Research Program, Faculty of Medicine, University of Helsinki, 00290 Helsinki Finland

[2]Department of Cell and Tissue Dynamics, Max Planck Institute for Molecular Biomedicine, 48149 Münster, Germany

[3]Department of Physics and BioInspired Institute, Syracuse University, Syracuse, NY, USA.

[4]Department Cell Biology of the Skin, Cologne Excellence Cluster on Cellular Stress Responses in Aging Associated Diseases (CECAD), Center for Molecular Medicine Cologne, University Hospital Cologne, University of Cologne, Joseph-Stelzmann-Str. 26, 50931 Cologne, Germany.

[5]Max Planck Institute for Molecular Biomedicine, 48149 Münster, Germany

[6]Cluster of Excellence for Aging-Associated Diseases, CECAD Imaging Facility Cologne, University of Cologne, Cologne, Germany.

[7]Turku Bioscience Centre, University of Turku and Åbo Akademi University, Turku, 20520, Finland

[8]Faculty of Science and Engineering, Cell Biology, Åbo Akademi University, Turku, 20520, Finland

[9]Turku Collegium for Science, Medicine and Technology (TCSMT), Turku, 20520, Finland

[10]Department of Life Technologies, University of Turku, FI-20520 Turku, Finland.

[11]InFLAMES Research Flagship Center, University of Turku, Turku, Finland.

[12]Helsinki Institute of Life Science, Biomedicum Helsinki, University of Helsinki, FI-00290 Helsinki, Finland

*These authors contributed equally

[§]These authors jointly supervised this work

carien.niessen@uni-koeln.de

mmanning@syr.edu

sara.wickstrom@mpi-muenster.mpg.de

**Abstract**

Generating and maintaining multilayered epithelia requires coordinated cell division, differentiation, and tissue architecture, yet how multilayering arises remains unclear. Using the developing mouse epidermis, we show that basal stem cells adopt distinct multilayering strategies depending on tissue mechanics. Early in development, the epidermis is fluid-like, allowing undifferentiated cells to move suprabasally through perpendicular divisions or basal detachment before differentiating. As the tissue matures and rigidifies, a mechanical barrier is established that only allows upward movement of basal cells that have committed to differentiation. The final step of this commitment requires Notch signaling that is triggered by increased tissue stiffness and jamming, orchestrating a feedback loop that induces cell upward motion precisely when the bottom layer becomes crowded. Together, our findings identify tissue mechanics as the key determinant of how tissues drive multilayering and reveal mechanically regulated Notch signaling as a driver of epithelial delamination.

## Introduction

Stratified epithelia such as the skin epidermis are multilayered tissues where the basal layer consists of undifferentiated stem cells adhering to the basement membrane, while the suprabasal layers contain post-mitotic, differentiated cells [1-3]. Unlike other dynamically self-renewing epithelia such as the intestine, where clear tissue-scale geometric cues such as curvature compartmentalize the stem cell niche and differentiated progeny [4], it remains unclear how stratified epithelia establish and organize this spatial organization and differentiation dynamics during development and into adulthood.

To initiate or maintain epidermal stratification, stem cells that are restricted to the basal layer generate suprabasal cells via two distinct strategies: perpendicular divisions or detachment from the basal layer, termed delamination [2, 3, 5]. Early in development, proliferation rates in the epidermis are high - to match the rapid growth of the organism it covers, and to generate sufficient suprabasal cells for efficient establishment of a functional life-essential barrier [6]. During this period, perpendicular cell divisions generate suprabasal daughter cells [7]. In contrast, during adult homeostasis differentiation is independent of cell divisions, with cells moving suprabasally to replenish the most superficial, desquamating cornified layers, followed by parallel divisions of to maintain basal cell density [8, 9]. Key open questions remain: When and how does this switch in strategies occur? And how is upward movement robustly regulated, so that stem cells are retained in the basal layer while differentiating move

66 at the correct rates, maintaining basal layer density and epithelial thickness in the absence of
67 obvious signals like morphogens or tissue curvature?

68 Here we demonstrate that multilayering strategy is controlled by a mechanical barrier that is
69 established during development and hinders basal cells from moving upward. We establish a
70 new approach to quantitively measure this mechanical barrier by combining a 3D biophysical
71 model for cell and tissue mechanics with imaging of cell and tissue geometries in the basal
72 layer and at the basal-suprabasal interface. We find that at early developmental stages,
73 embryonic (E) day 13.5/14.5, there is little mechanical distinction between basal and
74 suprabasal layers, allowing basal cells to easily place cells suprabasally either through
75 perpendicular division or through rapid detachment assisted by fluctuations from cell
76 divisions. Starting around E15.5, a mechanical energy barrier between the basal and
77 suprabasal layers emerges, with cell divisions becoming mostly parallel and daughters not
78 crossing the barrier. Instead, basal cells must now undergo profound transcriptional
79 reprogramming– e.g. commit to delamination – in order to cross the barrier. How is this
80 decision to commit regulated? Our data suggests an elegant feedback mechanism involving
81 Notch signaling and tissue crowding. We show that Notch activation is sensitive to cell
82 shapes and tissue rigidity. Tissue crowding-induced changes trigger a transient Notch signal
83 in a small subset of cells, causing these cells to execute a transcriptional switch to complete
84 delamination. Collectively, our study shows that changes in tissue mechanics that drive
85 intercompartment boundary formation are essential determinants for a switch from early
86 embryonic to a mature differentiation and multilayering strategy. Moreover, we identify
87 Notch signaling as an integrative feedback relay to coordinate tissue density and cell fate
88 dynamics to correctly time the transition between the mechanically separated basal and
89 suprabasal compartments within a mature stratified epithelium.

90

91 **Results**

92 **Basal cells employ distinct embryonic stage-specific strategies to generate and**
93 **compartmentalize suprabasal layers**

94 To understand which mechanisms are used for epidermal multilayering, we employed a
95 whole embryo live imaging system [10, 11] to visualize long term (over 8 h) cell dynamics at
96 E14.5 and E15.5 (Fig. 1A). While perpendicular divisions were prevalent at E14.5, parallel
97 oriented cell divisions became predominant at E15.5 with the overall frequency of cell
98 divisions decreasing (Fig. 1B). As reported [12], cell divisions also occurred suprabasally at
99 E14.5 but much less at E15.5 (Fig. 1B, Supplementary Fig. 1A). Imaging of fixed tissues

showed that significantly more undifferentiated cells were found in the first suprabasal layer at E14.5 than at E15.5 (Supplementary Fig. 1B), as detected by Keratin (K)-14 expression that marks undifferentiated stem cells and K10 that marks differentiated suprabasal cells [13]. A fraction of these suprabasal undifferentiated cells were still proliferating at E14.5 but not at E15.5 (Fig. 1C). This suggested that differentiation is not associated with upward movement at early stages.

We then asked whether cell delamination itself also changed as a function of developmental stage. At E14.5, detachment of cells from the basement membrane was regularly observed, with upward movement lasting around 120 minutes. This detachment was frequently associated with a cell division, either occurring after a perpendicular division or followed by a mitosis in the suprabasal layer (Fig. 1D; Supplementary Movie 1). In contrast, at E15.5 delaminations were substantially slower, lasting at least 300 minutes, and were not associated with divisions (Fig. 1E; Supplementary Movie 2). The geometry of delaminating cells also changed; at E14.4 cells rounded up for delamination, while at E15.5 cells transitioned instead into elongated and basally constricted, wedge-like shapes prior to delamination (Fig. 1F), indicating a switch in mechanical state.

To better understand how these changes in division and delamination strategies relate to cell differentiation, and to identify the mechanisms involved, we turned to fixed tissue imaging. Previous work has implicated desmosomal cadherins/Desmoglein1 (Dsg1) in delamination [14]. At E14.5 no Dsg1 or K10-positive differentiating cells were detected in the basal layer (Fig. 1G). In contrast, at E15.5 Dsg1+ K10+ basal cells were now observed, indicating that these cells had already initiated commitment towards differentiation. These double-positive basal cells exhibited upregulation of Dsg1 with enhanced localization of Dsg1 (Fig. 1H) and E-cadherin (Supplementary Fig. 1C) at apical interfaces, displaying wedge-like shapes and nuclear deformation similar to delaminating cells seen in live imaging (Fig. 1H).

To precisely quantify the shape changes of these K10+-basal cells at E15.5, we performed super-resolution imaging of skin whole mounts. K10+ basal cells were still attached to the basement membrane as shown by staining for α6β4 integrins, (Fig. 1I), and displayed a wedge-like shape characterized by decreased basal adhesion length and increased apical adhesion surface (Fig. 1I). Interestingly, integrins were enriched at these narrow basal footprints, indicating that differentiation is initiated prior to complete cell detachment from the basement membrane (Fig. 1J).

Collectively, these experiments show that at early developmental stages embryos engage both perpendicular cell divisions and rapid delaminations associated with suprabasal divisions to

generate suprabasal layers. Instead, E15.5 and E16.5 embryos employ a substantially slower, division-independent delamination process associated with remodeling of cell adhesion and changes in cell shape to position cells suprabasally.

**A biophysical model predicts that in the presence of a mechanical boundary, delamination depends on the mechanical properties of the delaminating cell**

To understand the mechanistic basis for this switch in multilayering strategy, we turned to quantitative mechanical modelling. For this we developed 3D vertex model of the epidermis [11, 15] (see Supplementary Methods). The model consisted of suprabasal cells (brown), basal cells (light blue) and a basement membrane (dark blue; Fig. 2A). A key model feature was basal layer rigidity, governed by cell shape. We therefore parameterized this by $\Delta s$, the distance in shape space to the fluid-solid transition [15-17] (Fig. 2A, inset). The model also included heterotypic interfacial tensions between basal and adjacent suprabasal cells ($\sigma_a$; Fig. 2A, magenta), and a potentially wetting interfacial tension between basal cells and the basement membrane ($\sigma_b$ ; Fig. 2A green). A similar Voronoi-based model was recently used to study clonal dynamics of tumor cells in stratified epithelia {Sahu, 2025 #80}.

Previous work [11, 15] had shown that these three "tissue background" parameters ($\sigma_a$, $\sigma_b$, and $\Delta s$) generate a robust mechanical model that is capable of capturing key features of the multilayered tissue architecture observed *in vivo* by generating a mechanical boundary between the basal and suprabasal layers. This boundary ensures that small active mechanical fluctuations do not induce mixing between basal and suprabasal cells, and the layers are robustly separated, as observed at E15.5 onwards.

We sought to predict whether the presence of a mechanical boundary could explain the need for a mechanical change of the delaminating cell, observed at E15.5/E16.5 (see Fig, 1). We thus studied the behavior of a potential delaminating basal cell by altering specific interfacial tensions of this cell – lateral $\sigma_{dl}$, basal $\sigma_{db}$, and apical $\sigma_{da}$ (Fig. 2B). Past experimental observations [10, 18], suggested that basal layer rigidity $\Delta s$ is also relevant for delamination. We therefore also allowed it to vary while keeping the other "tissue background" parameters $\sigma_b$ and $\sigma_a$ fixed. We found that indeed, for a cell to move upward into the suprabasal layer in the presence of small active fluctuations, it needed only to change its interfacial tensions (Fig. 2C). We proceeded to precisely predict how changes to the mechanics of the delaminating cell alter the energy barrier and therefore the rates of delamination. To quantify these rates, we simulated a large ensemble of conditions (N>85) for each set of model parameters (3240

sets), and measured the fraction of cells that had delaminated in a fixed time window ($\Delta t$ = 2000 simulation time units, estimated to be 20 – 200 min [19, 20], see Supplemental Methods). We found that delamination rates are a complex function of the four variables ($\sigma_{da}$, $\sigma_{dl}$, $\sigma_{db}$, $\Delta s$; Supplementary Fig. 2A). In order to parse the resulting large parameter space, we adopted physics methodology [21] to search for a data collapse in delamination rates. We further tested if those rates were consistent with an Arrhenius process governed by an energy barrier, i.e. where the rate is proportional to $e^{-E/kT_{eff}}$, where $k\,T_{eff}$ sets the magnitude of active fluctuations [22-24]. We identified a specific combination of model parameters that generated a data collapse – i.e. where all delamination rate curves fell on top of one another (Fig. 2D; uncollapsed data in Supplementary Fig. 2). This indicated that a delaminating cell experiences a mechanical energy barrier to move upwards, and that this barrier can be modulated by the mechanical properties of the delaminating cell, in the following form:

$$E = F(\sigma_{da} - \sigma_{db} + c\,\Delta s)$$

Here $F$ is a monotonically increasing function of its argument (see Supplemental Methods). The first two terms indicate that the energy barrier depends on the difference between the basal and apical interface tensions of the delaminating cell. To decrease the energy barrier and delaminate more efficiently, a delaminating cell needs to increase the tension (i.e. decrease the wetting) with the basement membrane, while also decreasing its apical heterotypic interfacial tension with the suprabasal cells. This is consistent with the observed emergence of a wedge-like cell shape and apical Dsg1 enrichment observed in the experiments from E15.5 onwards (see Fig. 1G-I). The third term indicated that the energy barrier increases with increasing surrounding basal layer stiffness $\Delta s$. Interestingly, the energy barrier did not depend on $\sigma_{dl}$ - changes to the delaminating cell's lateral interfacial tension did not change the delamination rate (Fig. 2D). Overall, these results indicated that the non-mixing of basal and suprabasal cells observed at E15.5 and E16.5 is consistent with the existence of a mechanical energy barrier, and that cells can cross this barrier by changing their own mechanical properties.

**A substantial mechanical energy barrier emerges at E15.5 impacting delamination.**

Next, we sought to determine precisely if such a barrier emerges during development, and to quantify its impact on delamination. Previous work suggests that the apical curvature angle $\gamma$ and the cell height $h$ reflect a force balance along each interface [25, 26], and that interfacial

properties – lateral orientation $\beta$ and apical interface roughness $R$ - depend on heterotypic interfacial tensions [27, 28]. We therefore measured these observables and their variation *in vivo* in the basal layer (Fig. 3A-E) and integrated them with the 3D vertex model by converting the measurements to simulation units. We then simulated the model across a wide range of parameter conditions (Fig. 3F-M). For three observables ($R, \beta, h$), we discovered that the data could be collapsed as a simple function of the model parameters (Fig. 3F-K; Supplementary Fig. 3.A-C). As a result, the average value of each *in vivo* observable (Fig. 3F, H, J) specified a point on the y-axis of the respective simulation plot (Fig. 3G, I, K), and therefore generated a unique constraint on the model parameters. For $\gamma$ (Fig. 3L), force balance allowed us to quantify this directly as function of $\sigma_b$ and $\Delta s$ (Fig. 3M). This benchmarking process resulted in a set of four constraint equations for the three unknowns ($\sigma_b$, $\sigma_a$, $\Delta s$) at each developmental stage; we solved this system of equations for the best-fit model parameters at each stage using a standard over-constrained solver [29] (Fig. 3N; see Supplementary Methods).

These data demonstrated that at E14.5, the basal layer is nearly fluidlike, with very low tissue stiffness parameterized by $\Delta s$ (Fig. 3N). At this stage the interfacial tension between basal and suprabasal cells is low, coupled to a small, positive interfacial tension at the basement membrane interface, suggesting only low levels of integrin-based wetting. At E15.5, the tension at the basement membrane interface became negative, suggesting wetting behavior, accompanied by increased interfacial tension at the basal-suprabasal interface, as well as increased basal layer stiffness. At E16.5, similar trends remained, while tissue stiffness increased further (Fig. 3N). Combined, these changes generated a four-fold increase in the magnitude of the mechanical energy barrier for a basal cell to delaminate from E14.5 to E15.5 (Supplementary Fig. 3F-H).

This substantial increase in the mechanical barrier between E14.5 and E15.5 has important implications for strategies for delamination. Building upon our understanding from the data collapse in Fig. 2, we were then able to collapse the rates of delamination as a function of the differences in the interfacial tensions between the delaminating cell and the background basal cells at the apical ($\Delta\sigma_{da,a}$) and basal ($\Delta\sigma_{db,b}$) interfaces (Fig. 3O; Supplementary Methods Fig. 3C, see Supplemental Methods). This analysis showed that at E14.5, the probability of a standard basal cell (0.0 on the x-axis of Fig 3O) delaminating during the time window $\Delta t$ was less than 20%, but only a small change in basal and apical tensions (~15%, 0.15 on the x-axis in Fig 3O) was sufficient to generate a massive increase in the delamination probability, increasing it to nearly 100% in the same time window. In contrast, at E15.5 and E16.5, a

234 basal cell must change its mechanical properties substantially (by more than 50%, 0.5 on the
235 x-axis of Fig. 3O) in order to generate a similar increase in delamination probability.

236 Collectively, these data indicate that a mechanical boundary forms between the basal and
237 suprabasal layers at around E15.5, thus requiring cells to have a robust mechanism to commit
238 to delamination and overcome this barrier, while such a mechanism is not necessary at E14.5.

239

240 **A committed basal population characterized by Notch activation emerges at E15.5**

241 To identify the molecular driver for this predicted mechanical state change required for
242 delamination at E15.5 and later, we investigated the evolution of epidermal cell states using
243 single cell RNA sequencing (scRNAseq; Fig. 4A). We obtained single-cell suspensions of
244 skin from E13.5, E14.5, E15.5. and E16.5 embryos, isolated and sequenced in parallel to
245 avoid batch effects. The quality-controlled and filtered dataset, obtained from 2 biological
246 replicates/stage, comprised of >15,000 cells/stage that were annotated based on known
247 marker genes (Fig. 4A; Supplementary Fig. 4A, B). Focusing on the epidermal (non-hair
248 follicle) clusters, we identified cycling and non-cycling basal cells as well as suprabasal cell
249 states (Supplementary Fig. 4C, D). Leiden clustering revealed that cell states were clustered
250 separately according to their developmental stage, indicating that key cell states (basal and
251 suprabasal cells) underwent substantial transcriptional changes in transcriptomes while
252 progressing through development (Fig. 4B).

253 Closer inspection of key differentiation genes such as *Krt1*, *Krtdap* and *Notch1* revealed that
254 at E14.5 their expression was restricted to the suprabasal cell populations. In contrast, at
255 E15.5 and E16.5 a subset of basal cells also showed expression of differentiation genes (Fig.
256 4C). To conclusively identify a committed basal cell population, we examined a Harmony
257 integrated dataset of E14.5-E16.5 epidermal cells. Leiden clustering of this integrated dataset
258 revealed a distinct population of cells characterized by expression of both basal stem cell
259 (e.g. *Trp63* and *Itga6*) and terminal differentiation genes (Supplementary Fig. 4E, F),
260 indicating that only from E15.5 onward, a subset of basal cells commit to differentiation.
261 Next to this hybrid transcriptional signature of differentiation and stemness, this subset of
262 committed basal cells also showed enhanced expression of the suprabasal adhesion proteins
263 E-cadherin and desmoglein (Fig. 4D), consistent with a downregulation in heterotypic
264 interfacial tension between the committed cell and suprabasal cells predicted by the model
265 (Fig. 2D and 3O).

266 As Notch activity has been shown to be critical for terminal differentiation in keratinocytes
267 [30], we examined Notch pathway activity specifically in the basal layer. Receptor-ligand
268 enrichment analyses (CellPhoneDB; [31] predicted increased basal activity of especially
269 Notch1-Jagged2 signaling from E15.5 onward (Fig. 4E). Indeed, immunofluorescence
270 analysis revealed that Notch activity (cleaved intracellular domain; N-ICD), was detected in
271 single cells only in the basal layer of E15.5 and E16.5 epidermis, but not at E14.5 (Fig. 4F,
272 G). Intriguingly, these Notch1-active cells were also positive for the differentiation marker
273 K10 and displayed a wedge-shaped morphology (Fig. 4F), indicating that these cells are
274 committed to differentiation and undergoing delamination.

275 Collectively these data indicated the emergence of a committed basal cell state characterized
276 by a hybrid profile of stemness and differentiation, a change in cell shape, a switch to a
277 suprabasal cell adhesion profile and Notch activity.

278 **Generation of the mechanical boundary at E15.5 is concomitant with stiffening of the**
279 **basement membrane and rigidification of the basal layer**

280 We hypothesized that maturation of the tissue and specifically the basement membrane could
281 drive the emergence of the mechanical barrier at E15.5. Combined analysis of the scRNAseq
282 data (Fig. 5A) and quantitative multiplex tissue imaging using Imaging Mass Cytometry [32],
283 revealed an increase in basement membrane maturation and cell-matrix adhesion (Fig.5A-C;
284 Supplementary Fig. 5A). Importantly, collagen IV, a key component of the basement
285 membrane that is essential for its rigidification and stabilization, was increased from E14.5 to
286 E16.5 (Fig. 5B-C), suggesting maturation of the BM from E14.5-16.5. In agreement, the
287 hemidesmosomal α6β4 integrin was also increased during this transition, and became more
288 and more confined to the epidermal-dermal junction (Fig. 5B, C; Supplementary Fig. 5A).
289 Consistently, atomic force microscopy-mediated force spectroscopy confirmed a significant
290 stiffening of the basement membrane from E14.5 to E16.5 (Fig. 5D).

291 Based on observations in other systems [10, 15-18, 33] we speculated that this change in
292 basement membrane mechanics promoted establishment of a mechanical barrier between
293 basal and suprabasal cells through rigidification of the basal layer. Analyses of actomyosin
294 tension by quantifying myosin phosphorylation (pMLC2) showed increased tension at apical
295 cell-cell junctions and specifically at the interface between basal and suprabasal cells at
296 E15.5 compared to E14.5 (Fig. 5E), indicating emergence of a mechanical barrier, providing
297 further support for the geometry-based apical tension inference (Fig. 3N). Furthermore,
298 analyses of cell shapes and tissue dynamics from live imaging showed that the cells in the
299 basal layer of E14.5 embryos were larger and more irregular shaped compared to cells at

300 E15.5 (Fig. 5F, G; Supplementary Movie 3). In agreement, at E15.5 cell density was
301 increased, (Fig. 5F, H), with decreased mobility of the basal layer cells as quantified by
302 particle image velocimetry (Fig. 5F, I; Supplementary Movie 3), in line with the geometry-
303 based basal tissue stiffness inference (Fig. 3N). Together, these changes were consistent with
304 a tissue-scale rigidity transition in the developing epidermis that occurs from E14.5-16.5,
305 from an initially floppier basement membrane and a fluid-like basal layer to a stiff basement
306 membrane and a jammed basal layer with enhanced cell-matrix adhesion and apical
307 actomyosin tension.

308

309 **Tissue rigidity and cell shape changes drive Notch-dependent delamination and control**
310 **of tissue crowding**

311 We next investigated whether the changes to tissue rigidity are sufficient to induce basal
312 layer jamming and the emergence of a mechanical barrier. For this we mimicked tissue
313 maturation *in vitro* by modulating cell density and substrate rigidity by engineering
314 micropatterned adhesive islands on polyacrylamide hydrogels of defined stiffness (Fig. 6A).
315 Culturing primary epidermal progenitors on micropatterned islands revealed that increasing
316 substrate stiffness under confinement not only substantially enhanced differentiation (Fig.
317 6B), but, importantly, promoted efficient separation of the undifferentiated basal and
318 differentiated suprabasal cell populations (Fig. 6C), indicative of boundary formation.

319 As the scRNAseq associated the emergence of committed cells with Notch activity (Fig. 4D),
320 we then asked whether basal layer crowding was sufficient to induce Notch signaling. For
321 this, we performed live imaging of primary epidermal progenitors isolated from Notch1
322 activity reporter mice [34] to identify emergence of Notch-active basal cells in cells triggered
323 to differentiate and form a suprabasal layer (Fig. 6D). As expected, all progenitors were
324 initially Notch-reporter negative, but upon application of calcium to trigger differentiation
325 and multilayering, individual cells gradually switched on the reporter followed by
326 delamination (Fig. 6D; Supplementary Movie 4). Intriguingly, prior to turning on Notch1
327 signaling these cells were more elongated and resided in denser tissue regions than reporter
328 negative-cells (Fig. 6D), thus indicating that crowding and increased cell-cell to cell-matrix
329 contact area promoted Notch activation.

330 We then asked whether Notch1 transcriptional activity is necessary for cell fate commitment
331 and delamination by deleting the Notch transcription factor, Rbpj, in the epidermis (Rbpj-
332 KO; [35, 36]). At E14.5, the epidermis of Rbpj-KO mice appeared largely comparable to
333 control littermates (Fig. 6E). At E15.5, and more prominently at E16.5, the epidermis became

334 structurally more abnormal, characterized by a specific thinning of the suprabasal
335 differentiated layers (Fig. 6F). Moreover, basal cells were increased in height and became
336 more columnar in E15.5 and E16.5 Rbpj-KO mice compared to controls (Fig. 6G),
337 accompanied by higher cell density (Fig. 6D), indicating increased crowding of the basal
338 layer. To examine if this increased crowding was due to reduced commitment to
339 differentiation or decreased delamination, we quantified differentiating, delaminating cells.
340 We observed emergence of the committed basal cell population in both control and Rbpj-KO
341 epidermis (Fig. 6H), indicating that the initial commitment to differentiate does not depend
342 on Notch activity. Instead, we observed an increase in the number of wedge-shaped
343 committed cells undergoing delamination at this stage (Fig. 6H), suggesting an inability to
344 overcome the mechanical energy barrier and move suprabasally.

345 To identify the molecular mechanism by which Notch transcriptional activity regulates
346 efficient delamination, we performed scRNAseq analysis across E14.5-E16.5 from control
347 and Rbpj-KO mouse skin. Overall, basal cell populations were transcriptionally similar
348 between controls and Rbpj-KO mice (Fig. 6I). However, as described previously [30], Rbpj-
349 KO cells of all developmental stages displayed impaired terminal differentiation (Fig. 6I;
350 Supplementary Fig. 6A). Intriguingly, at E15.5 a distinct Leiden cluster representing
351 committed basal cell population emerged, mainly composed of Rbpj-KO cells (Fig. 6I, J;
352 Supplementary Fig. 6B). Consistently, at E16.5 the Leiden cluster consisting of committed
353 cells was dominated by Rbpj-KO cells (Fig. 6I, J; Supplementary Fig. 6B), validating the
354 immunofluorescence observations that Rbpj-KO still commit to initial differentiation but
355 cannot efficiently delaminate, leading to accumulation of committed basal cells.

356 To identify master transcriptional switches downstream of Notch that drive the final step of
357 delamination, we performed differential gene expression analyses of committed cells between
358 control and Rbpj-KO at E15.5 and E16.5. This analysis identified two interesting
359 significantly altered regulators in Rbpj-KO committed cells: the zinc finger protein Zpf800, a
360 master regulator of intestinal stem cell differentiation [37], was not upregulated (Fig. 6K left
361 panel; Supplementary Fig. 6C, D). At the same time Rbpj-KO basal cells failed to
362 downregulate the Ep300 Inhibitor of Differentiation (Eid1) (Fig. 6K, right panel). Eid1 acts
363 as a transcriptional repressor through inhibition of p300-mediated H3K27 acetylation
364 (H3K27ac), thus preventing the activation of enhancers that promote differentiation [38, 39].
365 Indeed, RNA in situ hybridization and quantitative immunofluorescence confirmed that while
366 control embryos downregulated Eid1 in the suprabasal layers and, as a consequence, showed
367 substantially reduced H3K27ac levels in delaminating cells and suprabasally, Rbpj-KO

368 embryos maintained both high Eid1 and H3K27ac in delaminating cells and suprabasal
369 layers, in line with reduced differentiation (Fig. 6L).

370 Collectively, these data demonstrate that stiffening of the substrate is sufficient to drive basal
371 layer jamming and the formation of a mechanical barrier between basal and suprabasal
372 compartments. This basal layer jamming and crowding then triggers Notch signaling required
373 for completion of delamination and control of basal layer density.

374

375 **Discussion**

376 Here we show that the developing epidermis employs different strategies for multilayering
377 that are driven by changes in tissue mechanics. Early during development of this stratified
378 epithelium, there is no substantial energy barrier between basal and suprabasal cell layers.
379 This allows fast upward movement of basal cells independent of basal fate commitment by
380 either dividing perpendicularly or detaching quickly in order to rapidly establish a stratified
381 tissue. At later stages (E15.5 and beyond), maturation and stiffening of the basement
382 membrane enhance basal cell-matrix adhesion and crowding to rigidify the tissue. This
383 results in the generation of a substantial mechanical energy barrier between basal and
384 suprabasal cells. In order to cross this barrier, cells must commit to differentiation and
385 undergo subsequent transcriptional rewiring, controlled by Notch activation, to complete
386 delamination. Interestingly, this delamination process in the matured epidermis is
387 substantially slower than the rapid detachment observed by us and others in early embryonic
388 development [40]. As Notch activation itself is regulated by tissue rigidification and
389 crowding, it suggests an elegant control mechanism for homeostasis in an open niche, where
390 tissue crowding in a rigidified tissue triggers Notch activation to control the rate and timing
391 of delamination. This allows accurate control over the densities of both basal and suprabasal
392 layers.

393 Many open questions remain. A key open question is how the system decides which subset of
394 cells in the basal layer becomes committed and Notch active. Previous work has suggested
395 that since Notch is a surface receptor, its activity depends the cell shapes and surface areas
396 that regulate the density of such receptors [41, 42]. This could explain the emergence of
397 Notch active cells in elongated cells within dense regions – these cells would have transiently
398 maximized surface area to receive Notch ligand signal from their neighbors. Previous work
399 has investigated a 2D vertex model where cell fate decisions are coupled to cell areas [43],
400 which may be a useful starting point for predicting features we observe here. Future modeling
401 work should focus on understanding how changes to tissue stiffness and cell shape induce

402 Notch signaling in a 'correct' subset of basal cells (e.g. they are spaced out and the right
403 fraction depending on the degree of crowding), and on adding the effects of differently
404 oriented cell divisions in basal layer — in different developmental stages – to the 3D model.

405 Downstream of Notch signaling, it will be intriguing to understand how the transcriptional
406 reprogramming, involving Eid1and Zfp800 associated with global changes in H3K27ac
407 translates to control of delamination timing. It is interesting to note that the direct
408 downstream targets of Eid1- the histone acetyltransferases P300 and CBP - are evolutionarily
409 conserved maintenance factors of lineage-specifying core-transcriptional networks. They
410 function as transcriptional rheostats that control global H3K27ac levels, where the duration of
411 their activity determines the long-term impact on chromatin state [44, 45]. Upon their
412 inhibition, >8h of hypoacetylation is required to trigger a permanent switch and "point of no
413 return" to H3K27me3-mediated chromatin silencing [44]. Intriguingly, this is the
414 approximate duration of the slower delamination process after E15.5. Thus, Notch may
415 function as a mechanical sensor to ensure that terminal differentiation is not initiated
416 prematurely in areas of low basal cell density. Precise coordination of onset of terminal
417 differentiation with basal stem cell layer density is likely to be a critical feature in
418 dynamically self-renewing tissues with an "open stem cell niche". Collectively, we propose
419 that in such tissues mechanical boundaries are required to separate biological activities of
420 cycling stem cells and post-mitotic terminally differentiated cells. Here, precisely controlled
421 cell state transitions control the transit between the compartments to robustly maintain tissue
422 homeostasis and barrier integrity.

423

424 **Methods**

425 **Mice**

426 Membrane-targeted Tomato reporter mice ($R26R^{mT/mG}$), nucleus-targeted Tomato reporter
427 mice ($R26R^{nT/nG}$) and high-activity Notch1 activation-dependent reporter mice (N1IP: CreHI)
428 were from were from JAX laboratories (stock #007676, #:023035 and #027234 respectively).
429 Rbpj floxed mice were obtained from JAX (stock # 034200) and crossed with the K14-Cre
430 line [35] to obtain epidermis-specific depletion. Embryos were staged based on vaginal plug
431 (taken as embryonic day 0) and limb morphology. All mouse studies were approved and
432 carried out in accordance with the guidelines of the Ministry for Environment, Agriculture,
433 Conservation and Consumer Protection of the State of North Rhine-Westphalia (LANUW;
434 81-02.04.2022.A065; and 2024-155), Germany.
435

436 **Ex vivo embryo imaging**

437 Imaging was performed essentially as described earlier [10, 11]. Briefly, embryos were
438 dissected at embryonic stages E14.5 or E15.5 and immobilized on custom-built imaging
439 chambers engineered on top of Lumox-teflon imaging plates to allow gas exchange
440 (Sarstedt). Whole embryos were immersed in epidermal growth medium (CnT-PR,
441 CELLnTEC Advanced Cell Systems) supplemented with calcium-depleted 10% fetal bovine
442 serum (HyClone/Thermo Fisher), 20 U/ml penicillin-streptomycin (Thermo Fisher), 20 mM
443 Hepes, 1.8 mM CaCl2, and 10 ng/ml mouse recombinant EGF (Novus; NBP2-34952).
444 Imaging was performed using an Andor Dragonfly 505 high-speed spinning disk confocal
445 microscope (Oxford Instruments) with an inverted Nikon Eclipse Ti2 microscope (Nikon)
446 equipped with 488 nm and 546 nm lasers, an Andor Zyla 4.2 sCMOS camera and an
447 environmental chamber set at 37°C, 5% CO2 using a 40X dry objective. Images were
448 acquired using Fusion 2.0 software (Andor). After acquisition, the image series were 3D drift
449 corrected using the ImageJ plug-in Fast4Dreg [46] combined with manual registration, if
450 required.

451

452 **Immunofluorescence and confocal microscopy**

453 For skin whole mounts, embryos were dissected from pregnant mice and directly fixed in pre-
454 warmed (37°C) 4% paraformaldehyde (PFA) at room temperature for 3 h. After multiple PBS
455 washes, the skin was carefully peeled using forceps and placed in blocking solution (0.5%
456 Triton-X, 5% bovine serum albumin (BSA), 3% normal goat serum (NGS)) for 1 h at room
457 temperature. For paraffin sections tissue biopsies were fixed in 4% PFA, embedded in
458 paraffin and sectioned. Sections were de-paraffinized using a graded alcohol series and
459 antigen retrieval was carried out using target retrieval solution (Dako) at pH 6 or pH 9 in a
460 pressure cooker. For cryosections, tissue samples were placed unfixed into cryomolds,
461 embedded in OCT (Tissue Tek) and allowed to harden on dry ice. 8 µm thick sections were
462 cut, air-dried and fixed with 4% PFA. For both paraffin and cryofixed sections, samples were
463 blocked in 5% BSA, 3% NGS. For paraffin sections antibodies were diluted in Dako
464 antibody diluent (Agilent). For cryosections antibodies were diluted in blocking solution.
465 Cultured epidermal cells were fixed in 4% PFA for 15 min at room temperature After PBS
466 washes, samples were placed in 0.3% Triton-X, 5% BSA for one hour at room temperature
467 after which primary antibodies were diluted in the same solution. In all cases antibodies were
468 incubated overnight in moist chamber at 4°C. Following PBS washes, secondary antibodies
469 were diluted in 1% BSA in PBS and incubated for 1h at room temperature.

470

471 For super-resolution imaging of Dsg1, K10, E-cadherin, and Integrin α6, the embryos were
472 fixed in pre-warmed 4% PFA at 37°C for 1 hour and rinsed with PBS. The back skin was
473 peeled using forceps and incubated in blocking solution for 24 hours at 37°C. Primary
474 antibodies were diluted in the blocking solution and incubated 48 hours at 37°C on shaker
475 followed by several washes with 2% Triton-X with a final overnight wash. Secondary
476 antibodies were diluted in blocking solution and incubated 24 hours at 4°C followed by
477 several washes with 2% Triton-X.
478 For pMLC2 staining embryos were fixed in 4% PFA dissolved in HBSS for 1 hour on a
479 shaker at room temperature. Back skins samples are then peeled and permeabilized with
480 0.02% PBS-Tween 20 for 30mins and blocked with blocking solution (5% NGS,1% BSA) for
481 2 hours before incubating with primary antibody overnight in 4ºC. Samples are then
482 thoroughly washed with 0.02% PBS-Tween 20, incubated with secondary antibodies at 1:400
483 dilution for 1 hour at room temperature and washed. All tissue samples were mounted in
484 Elvanol.
485 The following primary antibodies were used: guinea-pig anti-Keratin 10 (Progen, #GP-10;
486 1/300); rabbit anti-p-MLC2 (p-Ser19; Cell Signaling, 3675; 1:200), rabbit anti-cleaved-
487 Notch1 (Cell signaling; #4147S; 1/50), mouse anti-Desmoglein 1/2 (Progen, #61002; 1/200),
488 rabbit anti-TGM1 (360; Proteintech, #12912-3-AP; 1/300), rabbit anti P63 (Genetex
489 #GTX102425; 1/100), guinea-pig anti-Keratin 14 (Progen, GP-CK14; 1:300). Bound primary
490 antibody was detected by incubation with Alexa-Fluor 488-, 568- or 647 -conjugated
491 antibodies (Invitrogen). Nuclei were counterstained with 4′, 6-diamidino-2-phenylindole
492 (DAPI, Invitrogen). Slides were mounted in Elvanol.
493 Fluorescence images were collected by laser scanning confocal microscopy (LSM980; Zeiss)
494 with with Zeiss ZEN Microscopy software (Zeiss ZEN version 3.7) using a 40X water
495 immersion objective. Images were acquired at room temperature using sequential scanning of
496 frames of 1 µm thick confocal planes (pinhole 1). Images were collected with the same
497 settings for all samples within an experiment. For super-resolution imaging a 63X oil
498 objective and the Airyscan 2 SR (super-resolution) mode with default resolution settings
499 were used. Laser power and image size were kept at a minimum to avoid photo-bleaching.
500 All airyscan images were 3D processed using the Zeiss Airyscan Processing mode with auto
501 filter and standard strength.
502
503 **Embryonic epidermal vertex analysis**
504 Membrane-tomato positive E14.5, E15.5 and E16.5 embryos were isolated, fixed
505 immediately in 4%PFA over night at 4°C and washed in PBS. The back skin was then

506 removed using micro-scissors and forceps and permeabilized in PBS/0.5% Triton-X for 1h at
507 RT. Nuclei were stained by incubating the skin in DAPI diluted in DAKO antibody diluent
508 for 1h at RT. The skin was then mounted in Mowiol.
509
510 Confocal stacks were recorded at a voxel size of X: 0.361, Y: 0361, Z:0.299 using a Leica
511 SP8 equipped with an APO CS2 63x/1.40 oil objective. To determine basal cell vertices,
512 confocal stacks were processed in Imaris and minimal XZ or YZ projection were exported
513 using the extended section view. Using the segmented line tool in ImageJ a line was drawn
514 across the apical and basal vertices of basal cells. Coordinates were extracted and "Julia" was
515 used in Visual Code Studio to determine cell height (h), apical and basal vertex distances (a)
516 and the lateral interface orientation (angle beta). The lines connecting the basal and apical
517 vertices, respectively, were used to determine the apical layer roughness (R) (See also
518 Supplementary Methods). The apical curvature angle gamma was determined manually using
519 the angle tool in ImageJ.
520
521 **Image analyses**
522 For tissue-scale analysis, 2D segmentation were performed from live imaging data on
523 whole embryos or cultured epidermal progenitor monolayers using Cellpose4SAM (v4.0.8)
524 [47]. 2D cell shape parameters were measured using custom Python script and cell densities
525 were measured using ImageJ. For analyses of cell shapes of delaminating cells from embryo
526 live imaging, Imaris 11 was used to manually create 3D surfaces of delaminating and
527 corresponding neighboring basal cells. Meshes were exported from Imaris surfaces after
528 which shapes were analyzed by quantifying Spherical Harmonics [48] using a custom Python
529 script.
530 In fixed tissue samples, basal committed cells and delaminations were identified based on the
531 expression of specific markers (K10 and/or Desmoglein) and their contact with the basement
532 membrane, and subsequently manually counted. Active-Notch positive cells were quantified
533 manually. The method was applied across all stages and conditions. Integrin $\alpha$6, E-cadherin
534 and Desmoglein mean intensities were manually measured at the basal, apical and lateral
535 membranes on Image J. To quantify epidermis thickness, the distance between epidermal
536 basement membrane and most superficial point of the epidermis was measured. To quantify
537 specifically the basal layer thickness versus the differentiated layer thickness, the expression
538 of specific markers (K10 and desmoglein) has been used to distinguish the differentiated
539 layers (K10+) from the basal layer.

To measure boundary straightness between the bottom and upper layers in micropatterns of soft and stiff polyacrylamide (PAA) hydrogels, both a segmented line following the top of each nucleus in the bottom layer and a straight line were drawn. The lengths of these lines were measured using ImageJ, and the ratio of the straight line to the segmented line was calculated.

Eid1 RNA signal was quantified by segmenting suprabasal cells based on Keratin-DAP–positive cells. Mean fluorescence intensity of Eid1 mRNA was measured using Fiji.

**3D vertex model**

A dynamic three-dimensional model of stratified epithelial tissues was developed using the 3D vertex framework (Zhang and Schwarz, 2022). In the 3D vertex model, cells are represented as polyhedra, each characterized by a homeostatic volume $V_0$ and surface area $S_0$. The geometry of each cell is defined by its vertices, which serve as the degrees of freedom of the system. The modeled epithelium consists of two main cell compartments. The upper compartment represents the suprabasal differentiated cell layer, while the middle one-cell-thick layer corresponds to the basal stem cell layer. Because the vertex model treats cells as space-filling polyhedra, we modeled the basement membrane as an additional layer of interconnected "cellular network" directly attached beneath the basal layer. In this framework, cells exert forces on one another through shape-based interactions governed by the following energy functional :

$$E = \sum_{\alpha} K_S (S_\alpha - S_0)^2 + \sum_{\alpha} K_V (V_\alpha - V_0)^2 + \sum_{\alpha\beta} \boldsymbol{\sigma}_{\alpha\beta} S_\alpha \quad (1)$$

The first term of the energy functional describes the competition between contractile forces generated by cell actomyosin networks (which enable cells to minimize their shape or surface area to resist their environments), and adhesive forces mediated by cadherin-based, which promote the elongation of cell–cell contacts during neighbors' exchange (T1s). The second term accounts for the mechanical resistance of cells to volume fluctuations, as most cells are fluid-filled and resist changes in volume. The third term incorporates heterotypic interfacial tension $\sigma_a$ between the basal cells and suprabasal cells, and the tension $\sigma_b$ associated with integrin-based wetting behaviors at basal-basement membrane interface.

Previous studies have shown that differential expression of adhesion molecules and cytoskeletal components associated with cell fate specification (through variations in protein or gene expression) can modify cell–cell interactions, leading to differences in adhesion strength and heterotypic interfacial tension [10, 11, 49-57]. Such tension differences are known

to play a central role in establishing and maintaining sharp tissue boundaries [55]. Moreover, basal cells adhere to the basement membrane via integrins, which introduce a wetting interaction characterized by $\sigma_b$ [58]. The parameters $K_S$ and $K_V$ denote the elastic moduli associated with the surface area and volume of the cells, respectively. Upon non-dimensionalization, this energy functional allows the definition of a key order parameter known as the target shape index, $s_0 = S_0 V_0^{-\frac{2}{3}}$, which controls the mechanical rigidity of the tissue. By tuning $s_0$, the epithelial confluent tissue exhibits a rigidity transition from a solid-like to a fluid-like state, with a critical value at $s_0 = 5.4$ [15, 17].

To quantitatively predict the mechanical parameters and cellular mechanisms underlying mechanical barrier formation between the basal and suprabasal layers, we first simulated the epithelium in the absence of cell delamination. The system evolves according to overdamped Langevin dynamics, where vertex positions are continuously updated to minimize the total mechanical energy:

$$\partial_t r_i = -\mu \nabla_i E_i + \sqrt{2D_t}\, \boldsymbol{\eta}(t). \qquad (2)$$

The left-hand side represents viscous drag forces, the first term on the right-hand side corresponds to interaction forces derived from the energy potential, and the second term represents thermal fluctuations in vertex positions $r_i$ . Here $\boldsymbol{\eta}$ is an uncorrelated stochastic Gaussian white noise with unit amplitude, $D_t = \mu k_B T_{\text{eff}}$ , where $\mu$ is the mobility (inverse frictional drag), $k_B$ Boltzmann constant, and $T_{\text{eff}}$ is an effective temperature parameter that sets the scale of the fluctuations. Unless otherwise noted, for our simulations we choose $\mu = 1$, $k_B = 1$ and $T_{\text{eff}} = 0.002$. This choice of $T_{\text{eff}}$ allows fluctuations of interface lengths but is not sufficient to generate diffusion or fluidity in the basal layer.

From the simulated model, we can compute the effective tensions governing different interfaces: a) The homotypic tension between basal cells $\sigma_{bb} = 4K_S \Delta s_b$ where $\Delta s = s_\alpha - s_0$ measures the basal layer stiffness (and $\Delta s = 0$ at the transition point); b) The effective heterotypic tension at the basal-suprabasal interface $\Gamma_a = 2\sigma_a + 2K_s(\Delta s_s + \Delta s_b)$, where $\Delta s_s$ the stiffness of the suprabasal layer; c) The effective wetting tension $\Gamma_{bm} = 2\,\sigma_b + 2K_s(\Delta s_b + \Delta s_m)$ between basal cells and the basement membrane (constituted of a cellular network with

605 a small shape parameter). Unless otherwise noted, $\Delta s_m = 0.26$, which ensures the basement
606 membrane remains very stiff and solid-like.
607
608 For more detailed description see Supplementary Methods.
609
610 **Single-cell RNA sequencing (scRNAseq)**
611 E13.5, E14.5, E15.5 and E16.5 embryos from wild type, control or K14Cre-RBP-J
612 floxed/floxed mice (two embryos/genotype/stages) were collected simultaneously and back
613 skins were peeled off. Single-cell suspensions were generated by enzymatic digestion by
614 incubating back skin tissues in a mixture of DNAse I (40 µg/ml), Liberase (0.125 mg/ml;
615 Roche Cat. NO. 05401119001), and papain (30 U/ml; Worthington) in Minimum Essential
616 Medium, Spinner modification (Gibco 11380) for 15 min (E13.5), 20 min (E14.5), 30 min
617 (E15.5) or 40min (E16.5) at 37°C followed by mechanical dissociation. The reaction was
618 stopped with 22% FBS and single cells were washed with FACS buffer (0.2% chelated FBS,
619 2 mM EDTA in 1x DPBS (Sigma Aldrich, D8537)). For wild type sequencing, cells were
620 labeled with BD Mouse Single-Cell Multiplexing Kit (Cat # 633793): E13.5 rep 1: Sample
621 Tag (ST) 1; E13.5 rep 2: ST 2; E14.5 rep1: ST 3; E14.5 rep2: ST 4; E15.5 rep1: ST 5; E15.5
622 rep2: ST 6; E16.5 rep1: ST 7, E16.5 rep2: ST 8. For K14Cre-Rbpj floxed and control
623 sequencing, surface biotinylation was used [59]. Briefly, cells were labeled with 50 µg/mL
624 EZ-Link sulfo-NHS-biotin (Thermo Fisher Scientific, 21217) on ice for 10 min, followed by
625 incubation in 0.6 µg/ml TotalSeq-A PE streptavidin hashtag antibodies (BioLegend) for 30
626 min on ice as follows: E14.5 Rbpj-KO 1: TotalSeq™-A0951 PE Streptavidin 405251 ; E14.5
627 Rbpj-KO 2: TotalSeq™-A0952 PE Streptavidin 405253; E14.5 control 1: TotalSeq™-A0953
628 PE Streptavidin 405255; E14.5 control 2: TotalSeq™-A0954 PE Streptavidin 405257; E15.5
629 Rbpj-KO 1: TotalSeq™-A0951 PE Streptavidin 405251 ; E15.5 control 1: TotalSeq™-
630 A0953 PE Streptavidin 405255; E15.5 control 2: TotalSeq™-A0954 PE Streptavidin 405257;
631 E16.5 Rbpj-KO 1: TotalSeq™-A0951 PE Streptavidin 405251 ; E16.5 Rbpj-KO 2:
632 TotalSeq™-A0952 PE Streptavidin 405253; E16.5 control 1: TotalSeq™-A0953 PE
633 Streptavidin 405255; E16.5 control 2: TotalSeq™-A0954 PE Streptavidin 405257. Labeled
634 cells were loaded on a microwell cartridge of the BD Rhapsody Express system (BD)
635 following the manufacturer's instructions. Single-cell whole transcriptome analysis libraries
636 were prepared according to the manufacturer's instructions using BD Rhapsody WTA
637 Reagent kit (633802; BD), except for the Rbpj-KO and control sample tag libraries in which
638 totalseq-ADT-oligo1 (5'-TGCTCTTCCGATCTTGGCACCCGAGAATTCCA-3') primer in
639 place of Sample Tag PCR1 and Sample Tag PCR2 primers during the Sample Tag library

640 amplification [59]. Libraries were sequenced on the Illumina NextSeq 500 using High Output
641 Kit v2.5 (150 cycles; Illumina) for 2 × 75-bp paired-end reads with 8-bp single index aiming
642 sequencing depth of >20,000 reads per cell for each sample.
643
644 **scRNAseq analyses**
645
646 *Read Data QC and Mapping*
647 Illumina sequencing results were demultiplexed and converted to FASTQ format using
648 Illumina's bcl2fastq software (version 2.20.0.422). For K14Cre-RBP-J floxed/floxed data a
649 custom demultiplexing script was used to assign barcodes to sample tags (rhapsody-
650 demultiplex with parameters '-w BD_CLS1_v2.txt BD_CLS2_v2.txt BD_CLS3_v2.txt -a
651 TGGCACCCGAGAATTCCA <fastq files> sample_tags.txt', and sample tags as described
652 above).
653
654 Preprocessed read data was aligned to the mouse reference genome (GRCm39) and counted
655 with STAR [60] (version 2.7.11b) through its single-cell functionality STARsolo, using the
656 following parameters:
657
658 WT: `--runThreadN 16 --soloType CB_UMI_Complex --soloCellFilter None --outSAMtype
659 BAM SortedByCoordinate --soloFeatures Gene GeneFull GeneFull_Ex50pAS --
660 soloAdapterSequence NNNNNNNNNGTGANNNNNNNNNGACA --soloCBmatchWLtype
661 1MM --soloCBposition 2_0_2_8 2_13_2_21 3_1_3_9 --soloUMIposition 3_10_3_17 --
662 soloCBwhitelist BD_CLS1_v2.txt BD_CLS2_v2.txt BD_CLS3_v2.txt --runRNGseed 1 --
663 soloMultiMappers EM --readFilesCommand zcat --outSAMattributes NH HI AS nM NM
664 MD jM jI MC ch CB UB GX GN`
665
666 K14Cre-RBP-J floxed/floxed: `--soloType CB_UMI_Complex --soloAdapterSequence
667 NNNNNNNNNGTGANNNNNNNNNGACA --soloCBposition 2_0_2_8 2_13_2_21
668 3_1_3_9 --soloUMIposition 3_10_3_17 --soloBarcodeReadLength 0 --soloCellFilter None --
669 soloCBwhitelist BD_CLS1_v2.txt BD_CLS2_v2.txt BD_CLS3_v2.txt --
670 soloCBmatchWLtype 1MM --soloUMIfiltering MultiGeneUMI_CR --soloUMIdedup
671 1MM_CR --outSAMtype BAM SortedByCoordinate --soloFeatures Gene GeneFull
672 GeneFull_Ex50pAS --soloMultiMappers EM --outSAMattributes NH HI AS nM NM MD jM
673 jI MC ch CB UB GX GN --outSAMmultNmax 1 --outMultimapperOrder Random --
674 runRNGseed 1 --outFilterScoreMin 30 --outFilterMatchNmin 15`

675

676 *Data Filtering, Normalisation, and Visualization*

677 Preprocessing of the feature-count-matrix output by STARsolo was largely performed within
678 the scanpy [61]ecosystem, with the exception of scran normalization [62], which was
679 performed in R (R Core Team, 2017). All visualization was done using [63] functions.
680 Default parameters were used unless detailed otherwise.

681

682 For wild type:
683 Barcodes with less than 3000 UMI were discarded.
684 Only barcodes with less than 15% of counts stemming from mitotic genes were retained.

685

686 For K14Cre-RBP-J floxed/floxed and control:
687 Barcodes with less than 2000 UMI were discarded.
688 Only barcodes with less than 20% of counts stemming from mitotic genes were retained.
689 Only barcodes with less than 70% of counts stemming from hemoglobin genes were retained.
690 And barcodes were filtered for a complexity value above 0.75, where complexity is defined
691 as the log10-transformed number of expressed genes divided by the log10-transformed
692 number of total counts per barcode. Scran was used for normalization.

693

694 The separate samples were merged into a single object, G2M and S phase scores were
695 assigned to each cell using gene lists from [64] and the scanpy
696 scanpy.tl.score_genes_cell_cycle function, and regressed out of the gene expression matrix
697 using sc.pp.regress_out. 3000 highly variable genes were calculated from the normalized
698 matrix (sc.pp.highly_variable_genes, flavor "seurat"), and the first 100 principal components
699 were calculated with scanpy. Neighbourhood graph calculation (30 neighbors), UMAP
700 dimensionality reduction [65], and Leiden clustering [66] were performed. scrublet [67]
701 and/or scDblFinder were then used for doublet prediction.

702

703 Contaminant or undesired cell populations such as clusters of cells that, either manually or by
704 scrublet/scDblFinder, could be classified as doublets based on their expression patterns, were
705 removed. For this, cells were clustered at resolution 0.05, and the cluster corresponding to the
706 epidermal cells were isolated. These were then reclustered at resolution 0.1 (wild type) and
707 0.2 (K14Cre-RBP-J floxed/floxed) as described above, and undesired clusters were removed.
708 Finally, PCA, nearest neighbor calculation, and UMAP dimensionality reduction were
709 repeated for the clean epidermis data. For WT, stages E14.5, E15.5, and E16.5 were

710 additionally analysed separately with batch-correction using Harmony [68] after cell-cycle
711 regression.
712
713 *Differential expression analysis*
714 Differentially expressed genes were calculated using a pseudobulk approach [69], comparing
715 aggregate counts with 2 pseudoreplicates for each condition (pyDeSEQ2 0.4.8).
716
717 *Ligand-receptor interaction analysis*
718 We used CellphoneDB (v2.1.7 [31] with default parameters to analyse ligand-receptor
719 interactions. Mouse gene names were converted to human gene names prior to the analysis.
720
721 *Gene Set Enrichment Analysis*
722 We ranked differential expression results by pyDESeq2 shrunken log2-fold changes and used
723 GSEApy (v1.0.6 [70]) "prerank" to calculate the enrichment statistics.
724
725 **Imaging Mass Cytometry**
726 Primary antibodies from bovine serum albumin (BSA)- and azide-free formulations were
727 conjugated using the Maxpar X8 Labeling Kit (Standard BioTools) according to the
728 manufacturer's protocol. Stainings were performed on frozen cryosections according to the
729 manufacturer's protocol (Fluidigm). Briefly, 5 µm cryosections were prepared and stored at
730 −80 °C until use. On the day of the experiment, slides were equilibrated at −20 °C for 1 h and
731 then fixed in 4% paraformaldehyde (PFA) for 30 min at 4 °C. After washing in PBS, sections
732 were incubated in blocking solution (3% BSA) for 45 min at room temperature, followed by
733 incubation with the antibody cocktail prepared in 0.5% BSA for 1 h in a hydration chamber at
734 room temperature. Slides were then rinsed in 0.2% Triton X-100/PBS, stained with Cell-ID
735 Intercalator-IR (Fluidigm #201192A) for 30 min at room temperature, washed in Milli-Q
736 water, air-dried for 30 min, and stored until imaging. The samples were laser-ablated at 200
737 Hz using a Hyperion imaging mass cytometry system (Fluidigm) coupled to a Helios time-of-
738 flight mass cytometer with a resolution of 1 µm. Raw MiniCAD Design (MCD) files
739 generated by the Hyperion Imaging System were first inspected using the MCD Viewer
740 (Standard BioTools) to verify signal intensity and overall acquisition quality, and then
741 exported as TIFF images for downstream analysis on Image J. ROIs delineating the basement
742 membrane were drawn, and signal intensity at the basement membrane was measured using
743 ImageJ software.
744

745 **Atomic Force Microscopy**

746 For Atomic Force Microscopy (AFM), embryonic skin was dissected, immediately nitrogen
747 frozen and then embedded in OCT blocks. AFM measurements of the basement membrane
748 were performed on freshly cut 20 µm-thick cryosections using JPK Nano Wizard IV (Bruker
749 Nano) atomic force microscope mounted on an Olympus IX73 inverted fluorescent
750 microscopy (Olympus) and operated via JPK SPM Control Software v.5. Cryosections were
751 equilibrated in PBS supplemented with protease inhibitors and measurements were
752 performed within 20 minutes of thawing the samples. Triangular non-conductive Silicon
753 Nitride cantilevers (MLCT, Bruker Daltonics) with a nominal spring constant of 0,07 $Nm^{-1}$
754 were used for the nanoindentation experiments. For all indentation experiments, forces of up
755 to 3 nN were applied, and the velocities of cantilever approach and retraction were kept
756 constant at 10 $\mu m^{s-1}$ ensuring an indentation depth of 500 nm. All analysis were performed
757 with JPK Data Processing Software (Bruker Nano). Prior to fitting the Hertz model corrected
758 by the tip geometry to obtain Young's Modulus (Poisson's ratio of 0.5), the offset was
759 removed from the baseline, contact point was identified, and the cantilever bending was
760 subtracted from all force curves. Force curves were filtered for quality and all valid forces
761 curves were analyzed.
762
763

764 **Particle Imaging Velocimetry (PIV)**

765 PIV analysis of whole-embryo live imaging was performed as previously described, with
766 minor adjustments [11]. Briefly, prior to analysis, each movie was processed as follows: a 3D
767 drift correction was applied using the Fast4DReg plug-in in Fiji and sagittal cross-sections
768 containing the basal layers were selected. A median filter of 2 pixels was applied in Fiji,
769 followed by background subtraction using a rolling ball radius of 50 pixels.The movies were
770 then imported into PIVLab version 2.62. Tissue flow tracking was restricted to the
771 interfollicular epidermis. To exclude the hair follicle placodes from the analysis, ROIs
772 covering the placodes were manually drawn on the raw images and imported into PIVLab.
773 These masks were overlaid onto the flow field to exclude the placode regions. To prevent
774 tracking errors due to intensity variations, image contrast was enhanced using CLAHE
775 (Contrast Limited Adaptive Histogram Equalization) with a box size of 64 pixels. Denoising
776 was performed using a Wiener Noise Filter with a maximum pixel count of 3. Tissue flow
777 tracking was carried out using a multi-pass, windowed FFT-based approach, with window
778 sizes of 64 and 32 pixels for the first and second passes, respectively, and a 50% overlap. The

779 resulting vector fields were visually inspected, and any erroneous vectors were manually
780 removed from the analysis.
781
782 **Culture of primary epidermal progenitor cells**
783 Primary epidermal cells were isolated from newborn mice essentially as described [11].
784 Briefly, after dissection, skins were treated with antibiotic/antimycotic solution (Sigma
785 A5955) for 5 min, and epidermal single cell suspensions were generated by incubating skin
786 pieces in 0.8% trypsin for 30 min at 37 °C. Cells were suspended in Keratinocyte Growth
787 Medium (MEM Spinner's modification (Sigma), 5 µg/ml insulin (Sigma), 10 ng/ml EGF
788 (Sigma), 10 µg/ml transferrin (Sigma), 10 µM phosphoethanolamine (Sigma), 10 µM
789 ethanolamine (Sigma), 0.36 µg ml/ml hydrocortisone (Calbiochem), 2 mM glutamine
790 (Gibco), 100 U ml/ml penicillin, 100 µg ml/ml streptomycin (Gibco), 10% chelated fetal calf
791 serum (Gibco), 5 µM Y27632, 20 ng ml/ml mouse recombinant vascular endothelial growth
792 factor (VEGF) and 20 ng ml/ml human recombinant fibroblast growth factor-2 (FGF-2) (all
793 from Miltenyi Biotec) and seeded on cell culture plates coated with 30 µg $ml^{-1}$ collagen I
794 (Millipore) and 10 µg $ml^{-1}$ fibronectin (Millipore) for 1 h at 37 °C.
795
796 **Micropatterned hydrogels**
797 Circular micropatterns (100 µm diameter) were generated on glass coverslips activated by
798 oxygen plasma treatment for 3 min (PDC-002-CE Expanded Plasma Cleaner), as described
799 previously [10]. Activated coverslips were incubated with 1× PLL (Surface Solutions) for 30
800 min at room temperature, rinsed with 10 mM HEPES (pH 7.8), and subsequently incubated
801 with PEG-SVA (50 mg/ml in 10 mM HEPES, pH 7.8) for 1 h at room temperature.
802 Coverslips were rinsed with Milli-Q water and air-dried before patterning by deep-UV
803 (Primo; Alveole). PEG-cleaved regions were rinsed with Milli-Q water and incubated with 50
804 µg/ml fibronectin for 30 min at room temperature. In parallel, glass-bottom plates (Ibidi,
805 #81218-200) were silanized. Polyacrylamide gels of defined stiffness were prepared by
806 placing a drop of acrylamide/bis-acrylamide solution between the micropatterned coverslip
807 and the silanized plate. After 45 min of polymerization, the coverslip was removed,
808 transferring the ECM micropatterns onto the gel surface. Primary epidermal progenitors were
809 then seeded onto the patterned hydrogels.
810
811 **Live imaging of epidermal progenitor monolayers**
812 Freshly isolated epidermal progenitors isolated from N1IP: CreHI reporter mice crossed with
813 $R26R^{mT/mG}$ mice to label the plasma membrane and detect Cre activity were grown to

814 confluency in Keratinocyte Growth Medium and plated on 35 mm glass bottom dish with 14
815 mm micro-well plates (Cellvis; D35-14-1.5-N). Upon confluency, 200 μM $Ca^{2+}$ was added to
816 induce differentiation. Imaging was performed using an Andor Dragonfly 505 high-speed
817 spinning disk confocal microscope (Oxford Instruments) with an inverted Nikon Eclipse Ti2
818 microscope (Nikon) equipped with 488 nm and 546 nm lasers, an Andor Zyla 4.2 sCMOS
819 camera and an environmental chamber set at 37°C, 5% CO2 using a 40X dry objective.
820 Images were acquired using Fusion 2.0 software (Andor) with multiple positions and drift
821 stabilizer.

822

823 **RNA in situ hybridization**

824 RNA in situ hybridization was performed using RNAscope technology according to the
825 manufacturer's instructions (ACD, RNAscope Multiplex Fluorescent v2 Assay, kit:
826 RNAscope Multiplex Fluorescent v2 Assay ACD, #323100). Briefly, paraffin-embedded
827 tissue sections (5 μm thick) were deparaffinized in xylene, rehydrated through an ethanol
828 series, and incubated in hydrogen peroxide for 10 min at RT. Sections were then subjected to
829 antigen retrieval in RNAscope Target Retrieval solution for 15 min at 100°C using a pressure
830 cooker. RNAscope Protease Plus (ACD; #322331) was applied to each section and incubated
831 at 40°C for 30 min. The Eid1 RNAscope probe (ACD; #1713581-C3) and Keratin-DAP
832 RNAscope probe (ACD; #500671-C1) were hybridized according to the manufacturer's
833 protocol using the RNAscope Multiplex Fluorescent v2 Assay (ACD; #323100), followed by
834 signal detection with TSA Plus Fluorescein (Akoya, #NEL741001KT), TSA Plus Cyanine 3
835 System (Akoya, #NEL744001KT). All hybridization and amplification steps were performed
836 in a HybEZ II oven (ACD). DAPI solution was incubated for 30 seconds at room
837 temperature. Sections were mounted in Elvanol and imaged using a Zeiss LSM 980 confocal
838 microscope equipped with a 40× water-immersion objective, using Zeiss ZEN software
839 (version 3.5).

840

841 **Statistics and reproducibility**

842 Statistical analyses were performed using GraphPad Prism software (GraphPad, version 9) or
843 in R (version 4.2.2). Statistical significance was determined by the specific tests indicated in
844 the corresponding figure legends. Only 2-tailed tests were used. In all cases where a test for
845 normally distributed data was used, normal distribution was confirmed with the

Kolmogorov–Smirnov test ($\alpha = 0.05$). All experiments presented in the manuscript were repeated at least in 3 independent replicates.

## Data availability

Sequencing datasets are available at GEO (GSE315748 and GSE315746). All analysis scripts, custom code, and data that support the conclusions are available from the authors on request.


## Acknowledgements

We thank Claudia Ortmeier and Sandra Heising for expert technical assistance, Silvia Fre (Institute Curie, France) for advice on the project and general support, Fabien Bertillot for advice on image analyses, Yekaterina Miroshnikova for advice on micropatterning, and the Max Planck Institute BioOptics and Sequencing core facilities for support with experiments. Imaging Mass Cytometry was performed at the Cell Imaging and Cytometry Core, Turku Bioscience Centre (Turku, Finland), with the support of Biocenter Finland. This work was supported by European Union's Horizon 2020 research and innovation programme under Marie Skłodowska-Curie grant agreement no. 101032331 (to CV), Research Council of Finland (332402) and The Turku Collegium for Science, Medicine, and Technology (to GF), Academy of Finland Center of Excellence BarrierForce (346131) and R'Life Programme consortium NucleoMech (330033) (to JI and SAW) the Sigrid Juselius Foundation, Helsinki Institute of Life Science, and the Max Planck Society (all to SAW), NSF-CMMI-1334611 (to SA and MLM), grant number 2023-329572 from the Chan Zuckerberg Initiative DAF, an advised fund of the Silicon Valley Community Foundation (to MLM), and the Syracuse University Office of Research Future Faculty Fellow Program (to SA). CMN is supported by the Deutsche Forschungsgemeinschaft (DFG, German Research Foundation: Germany´s Excellence Strategy – EXC 2030 – 390661388; SPP 1782 NI 1234/6-2, Project-ID 388932620; FOR 2743 NI 1234/7-1 Project-ID 678823; ANR/DFG NI 1234/9 (Project-ID 505673300) and the European Union NETSKINMODELS, COST Action no. CA21108.


## Author contributions

CV, MA, and MR designed and performed experiments and analyzed data. SHAE and MLM developed vertex model and performed all simulations and analyses. KK performed

sequencing data analysis. SV and LCB supported live imaging and single cell sequencing experiments. AP performed and analyzed immunofluorescence experiments, PZ assisted with imaging. GF and JI performed mass cytometry experiment. CMN, MLM and SAW conceived and supervised the study, designed experiments, and analyzed data. MLM and SAW wrote the paper. All authors commented and edited the manuscript.

**Competing interests statement**

The authors declare no competing interests.

**References:**


1. Kulukian, A. and E. Fuchs, *Spindle orientation and epidermal morphogenesis.* Philos Trans R Soc Lond B Biol Sci, 2013. **368**(1629): p. 20130016.
2. Niessen, C.M., M.L. Manning, and S.A. Wickstrom, *Mechanochemical Principles of Epidermal Tissue Dynamics.* Cold Spring Harb Perspect Biol, 2025. **17**(6).
3. Tai, K., K. Cockburn, and V. Greco, *Flexibility sustains epithelial tissue homeostasis.* Curr Opin Cell Biol, 2019. **60**: p. 84-91.
4. Beumer, J. and H. Clevers, *Hallmarks of stemness in mammalian tissues.* Cell Stem Cell, 2024. **31**(1): p. 7-24.
5. Williams, S.E. and E. Fuchs, *Oriented divisions, fate decisions.* Curr Opin Cell Biol, 2013. **25**(6): p. 749-58.
6. Damen, M., et al., *High proliferation and delamination during skin epidermal stratification.* Nat Commun, 2021. **12**(1): p. 3227.
7. Lechler, T. and E. Fuchs, *Asymmetric cell divisions promote stratification and differentiation of mammalian skin.* Nature, 2005. **437**(7056): p. 275-80.
8. Cockburn, K., et al., *Gradual differentiation uncoupled from cell cycle exit generates heterogeneity in the epidermal stem cell layer.* Nat Cell Biol, 2022. **24**(12): p. 1692-1700.
9. Mesa, K.R., et al., *Homeostatic Epidermal Stem Cell Self-Renewal Is Driven by Local Differentiation.* Cell Stem Cell, 2018. **23**(5): p. 677-686 e4.
10. Miroshnikova, Y.A., et al., *Adhesion forces and cortical tension couple cell proliferation and differentiation to drive epidermal stratification.* Nat Cell Biol, 2018. **20**(1): p. 69-80.
11. Villeneuve, C., et al., *Mechanical forces across compartments coordinate cell shape and fate transitions to generate tissue architecture.* Nat Cell Biol, 2024. **26**(2): p. 207-218.
12. !!! INVALID CITATION !!! (Damen, Wirtz et al. 2021).
13. Moll, R., et al., *The catalog of human cytokeratins: patterns of expression in normal epithelia, tumors and cultured cells.* Cell, 1982. **31**(1): p. 11-24.
14. Nekrasova, O., et al., *Desmosomal cadherin association with Tctex-1 and cortactin-Arp2/3 drives perijunctional actin polymerization to promote keratinocyte delamination.* Nat Commun, 2018. **9**(1): p. 1053.
15. Zhang, T. and J.M. Schwarz, *Topologically-protected interior for three-dimensional confluent cellular collectives.* Physical Review Research, 2022. **4**(4): p. 043148.
16. Bi, D., et al., *A density-independent rigidity transition in biological tissues.* Nature Physics, 2015. **11**(12): p. 1074-1079.

17. Merkel, M. and M.L. Manning, *A geometrically controlled rigidity transition in a model for confluent 3D tissues.* New Journal of Physics, 2018. **20**(2): p. 022002.
18. Devany, J., et al., *Cell cycle-dependent active stress drives epithelia remodeling.* Proc Natl Acad Sci U S A, 2021. **118**(10).
19. Erdemci-Tandogan, G., et al., *Tissue Flow Induces Cell Shape Changes During Organogenesis.* Biophys J, 2018. **115**(11): p. 2259-2270.
20. Serwane, F., et al., *In vivo quantification of spatially varying mechanical properties in developing tissues.* Nat Methods, 2017. **14**(2): p. 181-186.
21. Somendra, M.B. and S. Flavio, *A measure of data collapse for scaling.* Journal of Physics A: Mathematical and General, 2001. **34**(33): p. 6375.
22. Bi, D., et al., *Energy barriers and cell migration in densely packed tissues.* Soft Matter, 2014. **10**(12): p. 1885-90.
23. McQuarrie, D.A., *Statistical Mechanics*. 1976, New York: Harper & Row.
24. Mombach, J.C.M., et al., *Rounding of aggregates of biological cells: Experiments and simulations.* Physica A: Statistical Mechanics and its Applications, 2005. **352**(534).
25. Maitre, J.L., et al., *Adhesion functions in cell sorting by mechanically coupling the cortices of adhering cells.* Science, 2012. **338**(6104): p. 253-6.
26. Pawlizak, S., et al., *Testing the differential adhesion hypothesis across the epithelial−mesenchymal transition.* New Journal of Physics, 2015. **17**(8): p. 083049.
27. Sahu, P., J.M. Schwarz, and M.L. Manning, *Geometric signatures of tissue surface tension in a three-dimensional model of confluent tissue.* New Journal of Physics, 2021. **23**(9): p. 093043.
28. Sahu, P., et al., *Small-scale demixing in confluent biological tissues.* Soft Matter, 2020. **16**(13): p. 3325-3337.
29. Press, W.H., et al., *Numerical Recipes: The Art of Scientific Computing*. 2020: Cambridge University Press.
30. Blanpain, C., et al., *Canonical notch signaling functions as a commitment switch in the epidermal lineage.* Genes Dev, 2006. **20**(21): p. 3022-35.
31. Efremova, M., et al., *CellPhoneDB: inferring cell-cell communication from combined expression of multi-subunit ligand-receptor complexes.* Nat Protoc, 2020. **15**(4): p. 1484-1506.
32. Giesen, C., et al., *Highly multiplexed imaging of tumor tissues with subcellular resolution by mass cytometry.* Nat Methods, 2014. **11**(4): p. 417-22.
33. Rustarazo-Calvo, L., et al., *Adhesion-driven tissue rigidification triggers epithelial cell polarity.* bioRxiv, 2025: p. 2025.03.18.644006.
34. Liu, Z., et al., *Notch1 loss of heterozygosity causes vascular tumors and lethal hemorrhage in mice.* J Clin Invest, 2011. **121**(2): p. 800-8.
35. Hafner, M., et al., *Keratin 14 Cre transgenic mice authenticate keratin 14 as an oocyte-expressed protein.* Genesis, 2004. **38**(4): p. 176-81.
36. Tanigaki, K., et al., *Notch-RBP-J signaling is involved in cell fate determination of marginal zone B cells.* Nat Immunol, 2002. **3**(5): p. 443-50.
37. Lin, L., et al., *Unbiased transcription factor CRISPR screen identifies ZNF800 as master repressor of enteroendocrine differentiation.* Science, 2023. **382**(6669): p. 451-458.
38. Miyake, S., et al., *Cells degrade a novel inhibitor of differentiation with E1A-like properties upon exiting the cell cycle.* Mol Cell Biol, 2000. **20**(23): p. 8889-902.
39. Witte, S., et al., *High-density P300 enhancers control cell state transitions.* BMC Genomics, 2015. **16**: p. 903.
40. Williams, S.E., et al., *Par3-mInsc and Galphai3 cooperate to promote oriented epidermal cell divisions through LGN.* Nat Cell Biol, 2014. **16**(8): p. 758-69.
41. Khait, I., et al., *Quantitative Analysis of Delta-like 1 Membrane Dynamics Elucidates the Role of Contact Geometry on Notch Signaling.* Cell Rep, 2016. **14**(2): p. 225-33.

42. Shaya, O., et al., *Cell-Cell Contact Area Affects Notch Signaling and Notch-Dependent Patterning.* Dev Cell, 2017. **40**(5): p. 505-511 e6.
43. Sarate, R.M., et al., *Dynamic regulation of tissue fluidity controls skin repair during wound healing.* Cell, 2024. **187**(19): p. 5298-5315.e19.
44. Hogg, S.J., et al., *Targeting histone acetylation dynamics and oncogenic transcription by catalytic P300/CBP inhibition.* Mol Cell, 2021. **81**(10): p. 2183-2200 e13.
45. Weinert, B.T., et al., *Time-Resolved Analysis Reveals Rapid Dynamics and Broad Scope of the CBP/p300 Acetylome.* Cell, 2018. **174**(1): p. 231-244 e12.
46. Pylvanainen, J.W., et al., *Fast4DReg - fast registration of 4D microscopy datasets.* J Cell Sci, 2023. **136**(4).
47. Pachitariu, M., M. Rariden, and C. Stringer, *Cellpose-SAM: superhuman generalization for cellular segmentation.* bioRxiv, 2025: p. 2025.04.28.651001.
48. Shen, L., H. Farid, and M.A. McPeek, *Modeling three-dimensional morphological structures using spherical harmonics.* Evolution, 2009. **63**(4): p. 1003-16.
49. Biggs, L.C., et al., *Mechanical Forces in the Skin: Roles in Tissue Architecture, Stability, and Function.* J Invest Dermatol, 2020. **140**(2): p. 284-290.
50. Dahmann, C., A.C. Oates, and M. Brand, *Boundary formation and maintenance in tissue development.* Nat Rev Genet, 2011. **12**(1): p. 43-55.
51. Foty, R.A. and M.S. Steinberg, *The differential adhesion hypothesis: a direct evaluation.* Dev Biol, 2005. **278**(1): p. 255-63.
52. Harris, T.J. and U. Tepass, *Adherens junctions: from molecules to morphogenesis.* Nat Rev Mol Cell Biol, 2010. **11**(7): p. 502-14.
53. Joost, S., et al., *Single-Cell Transcriptomics Reveals that Differentiation and Spatial Signatures Shape Epidermal and Hair Follicle Heterogeneity.* Cell Syst, 2016. **3**(3): p. 221-237 e9.
54. Krieg, M., et al., *Tensile forces govern germ-layer organization in zebrafish.* Nat Cell Biol, 2008. **10**(4): p. 429-36.
55. Monier, B., et al., *An actomyosin-based barrier inhibits cell mixing at compartmental boundaries in Drosophila embryos.* Nat Cell Biol, 2010. **12**(1): p. 60-9.
56. Rubsam, M., et al., *Adherens Junctions and Desmosomes Coordinate Mechanics and Signaling to Orchestrate Tissue Morphogenesis and Function: An Evolutionary Perspective.* Cold Spring Harb Perspect Biol, 2018. **10**(11).
57. Wickstrom, S.A. and C.M. Niessen, *Cell adhesion and mechanics as drivers of tissue organization and differentiation: local cues for large scale organization.* Curr Opin Cell Biol, 2018. **54**: p. 89-97.
58. Watt, F.M., *Role of integrins in regulating epidermal adhesion, growth and differentiation.* The EMBO Journal, 2002. **21**(15): p. 3919-3926.
59. Sugimoto, M., et al., *Universal Surface Biotinylation: a simple, versatile and cost-effective sample multiplexing method for single-cell RNA-seq analysis.* DNA Res, 2022. **29**(3).
60. Dobin, A., et al., *STAR: ultrafast universal RNA-seq aligner.* Bioinformatics, 2013. **29**(1): p. 15-21.
61. Wolf, F.A., P. Angerer, and F.J. Theis, *SCANPY: large-scale single-cell gene expression data analysis.* Genome Biol, 2018. **19**(1): p. 15.
62. Lun, A.T., K. Bach, and J.C. Marioni, *Pooling across cells to normalize single-cell RNA sequencing data with many zero counts.* Genome Biol, 2016. **17**: p. 75.
63. Hunter, J.D., *Matplotlib: A 2D Graphics Environment.* Computing in Science & Engineering, 2007. **9**(3): p. 90-95.
64. Tirosh, I., et al., *Dissecting the multicellular ecosystem of metastatic melanoma by single-cell RNA-seq.* Science, 2016. **352**(6282): p. 189-96.
65. McInnes, L.H., J.; Melville, J., *UMAP: Uniform Manifold Approximation and Projection for Dimension Reduction.* https://arxiv.org/abs/1802.03426}, , 2020.

66. Traag, V.A., L. Waltman, and N.J. van Eck, *From Louvain to Leiden: guaranteeing well-connected communities.* Sci Rep, 2019. **9**(1): p. 5233.
67. Wolock, S.L., R. Lopez, and A.M. Klein, *Scrublet: Computational Identification of Cell Doublets in Single-Cell Transcriptomic Data.* Cell Systems, 2019. **8**(4): p. 281-291.e9.
68. Korsunsky, I., et al., *Fast, sensitive and accurate integration of single-cell data with Harmony.* Nat Methods, 2019. **16**(12): p. 1289-1296.
69. Squair, J.W., et al., *Confronting false discoveries in single-cell differential expression.* Nat Commun, 2021. **12**(1): p. 5692.
70. Fang, Z., X. Liu, and G. Peltz, *GSEApy: a comprehensive package for performing gene set enrichment analysis in Python.* Bioinformatics, 2023. **39**(1).

## Main Figures

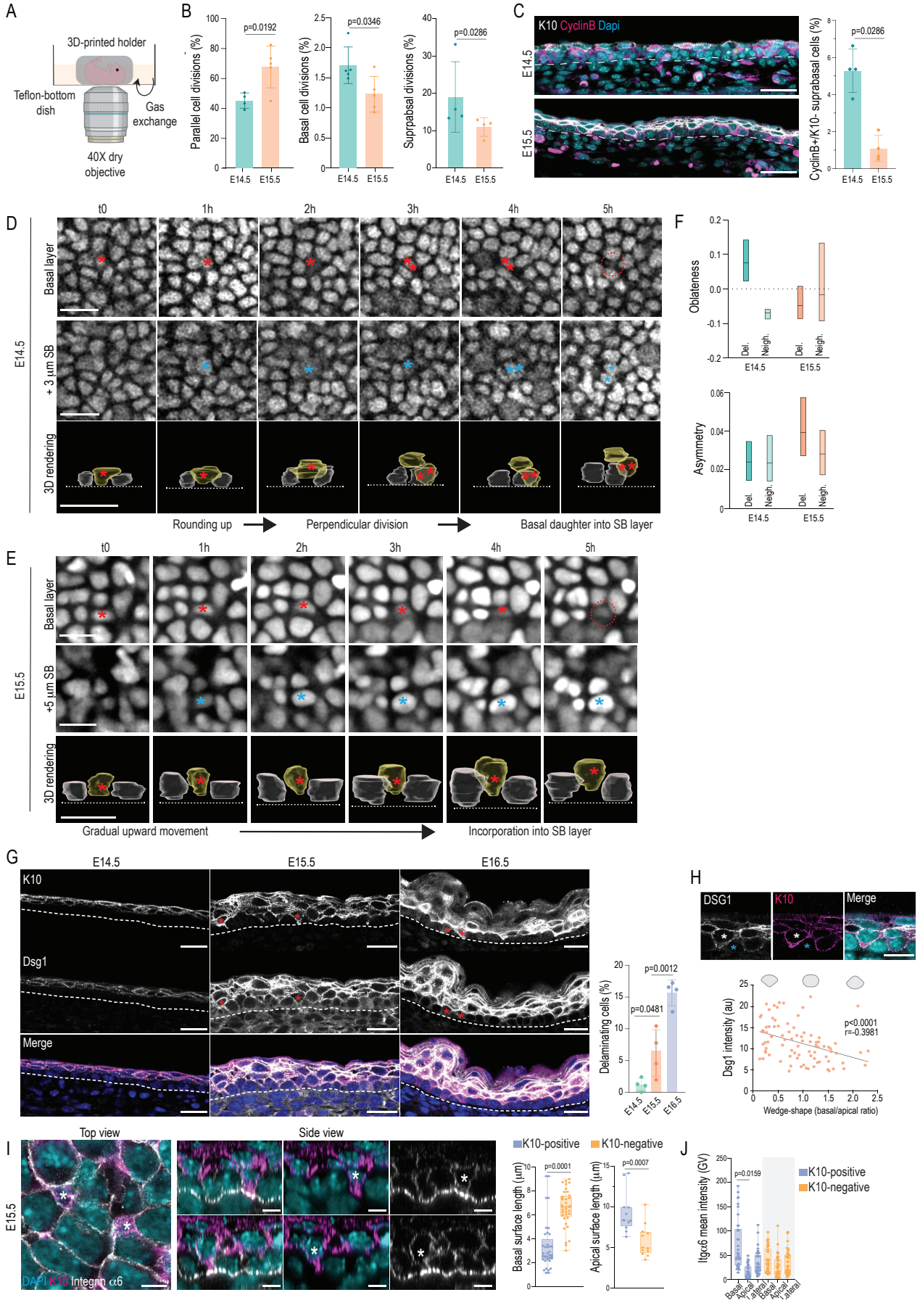


1040

1041 **Figure 1. Basal cells employ distinct embryonic stage-specific strategies to generate**

1042 **suprabasal layers**

1043 **A.** Schematics of the *ex vivo* embryo imaging setup. **B.** Quantification of parallel (left panel),
1044 basal (middle panel) and suprabasal (right panel) cell divisions in E14.5 and E15.5 embryos
1045 (mean ±SD; n=4 (E14.5) /5 (E15.5) embryos; Student's t-test (left and middle panel), Mann-
1046 Whitney (right panel)). **C.** Representative images and quantification of CyclinB-positive
1047 undifferentiated cells (K10-neg) in the suprabasal layers of E14.5 and E15.5 embryos (30
1048 µm; mean ±SD; n=4 embryos/stage; Mann-Whitney). **D.** Representative snapshots and 3D
1049 rendering (lower panel) from live imaging movies of E14.5 epidermis from nTomato reporter
1050 mice. Red asterisk marks cell departing from basal layer; double red asterisk marks daughter
1051 of perpendicular division that subsequently moves suprabasally, blue asterisks marks
1052 appearance of cells in the suprabasal layer, red dotted circle marks completed delamination.
1053 Images representative of 3 embryos, scale bars 20 µm. **E.** Representative snapshots and 3D
1054 rendering (lower panel) from live imaging movies of E15.5 epidermis from nTomato reporter
1055 mice. Red asterisk marks cell departing from basal layer; blue asterisk marks appearance of
1056 this cell in the suprabasal layer, red dotted circle marks completed delamination. Images
1057 representative of 3 embryos, scale bars 20 µm. **F.** Quantification of nuclear oblateness
1058 (roundness; upper panel) and asymmetry of deformation (wedge-shape; lower panel) of
1059 delaminating cells (Del.) and their immediate neighbors (Neigh.) from 3D renderings. Note
1060 that while at E14.5 delaminating cells round up, at E15.5 they elongate in an asymmetric
1061 manner (min-to-max box plots; n=3 embryos/stage). **G.** Representative images and
1062 quantification of tissue sections from E14.5 - 16.5 embryos stained against K10, Dsg1 and
1063 DAPI. Note emergence of K10-Dsg1- positive cells at 15.5 (red asterisks). Dotted line marks
1064 basement membrane (scale bars 20 µm; mean ±SD; n=4 embryos; Two-way
1065 ANOVA/Tukey's). **H.** Representative images and quantification of tissue sections from
1066 E15.5 embryos stained against K10, Dsg1 and DAPI. Note correlation of wedge-like shape
1067 and apical Dsg1 intensity. White asterisks mark wedge-like cells with high apical Dsg1, blue
1068 asterisks mark cuboidal neighboring cell (scale bars 10 µm; mean ±SD; n=87 cells pooled
1069 across 3 embryos; Simple linear regression; Pearson's correlation). **I, J.** Representative
1070 images and quantification of delaminating cells in E15.5 embryo 3D whole mounts stained
1071 against integrin α6 (Itga6), K10 and DAPI. Note wedge-like shape and integrin α6-positive
1072 basal footprint of the delaminating cell (white asterisks; scale bars 5 µm; min-max box and
1073 whiskers; n=37 cells pooled across 3 embryos; Mann-Whitney (left, middle panel)
1074 Friedman/Dunn's).

1075

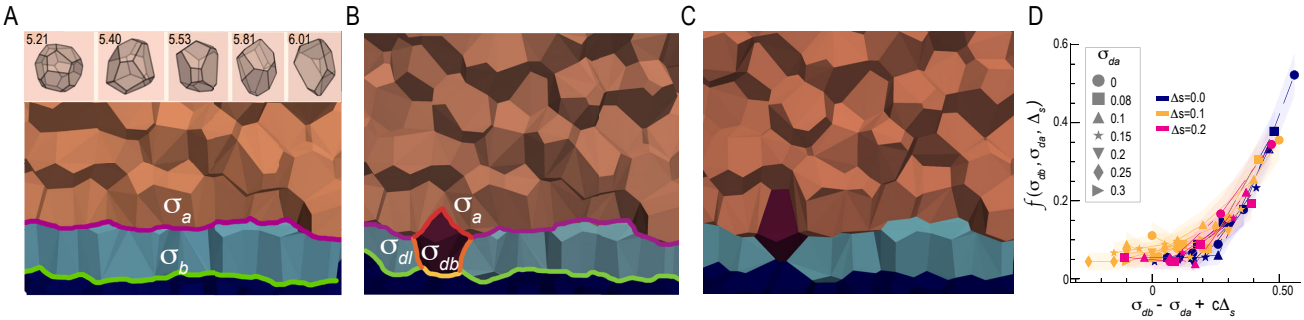


**Figure 2. A biophysical model predicts that in the presence of a mechanical barrier, delamination depends on the mechanical properties of the delaminating cell.**

**A.** Snapshot from 3D vertex model for stratified epithelium geometry, illustrating suprabasal cells (brown), basal cells (light blue) and basement membrane (dark blue), interfacial tensions between the apical surface of basal cells and the adjacent suprabasal cell ($\sigma_a$, magenta), basal cells and basement membrane ($\sigma_b$, green), and cell shapes (inset) with different 3D shape parameters. **B.** Simulation snapshot including a delaminating cell type, with potentially different delaminating cell-basal cell lateral interfaces $\sigma_{dl}$, delaminating cell-basement membrane interfaces ($\sigma_b$, yellow), and delaminating cell-suprabasal cell interfaces ($\sigma_{da}$, red). **C.** Snapshot of simulation showing cell in process of delaminating (cell integrates fully into the suprabasal layer by end of simulation). **D.** Fraction of cells that delaminate after a time t = X, as a function of $\sigma_{db}$, for many different values of the other parameters. Data averaged over an ensemble of n=20 simulations for each simulation condition. **E.** Delamination fraction collapses as a specific function of vertex model parameters.

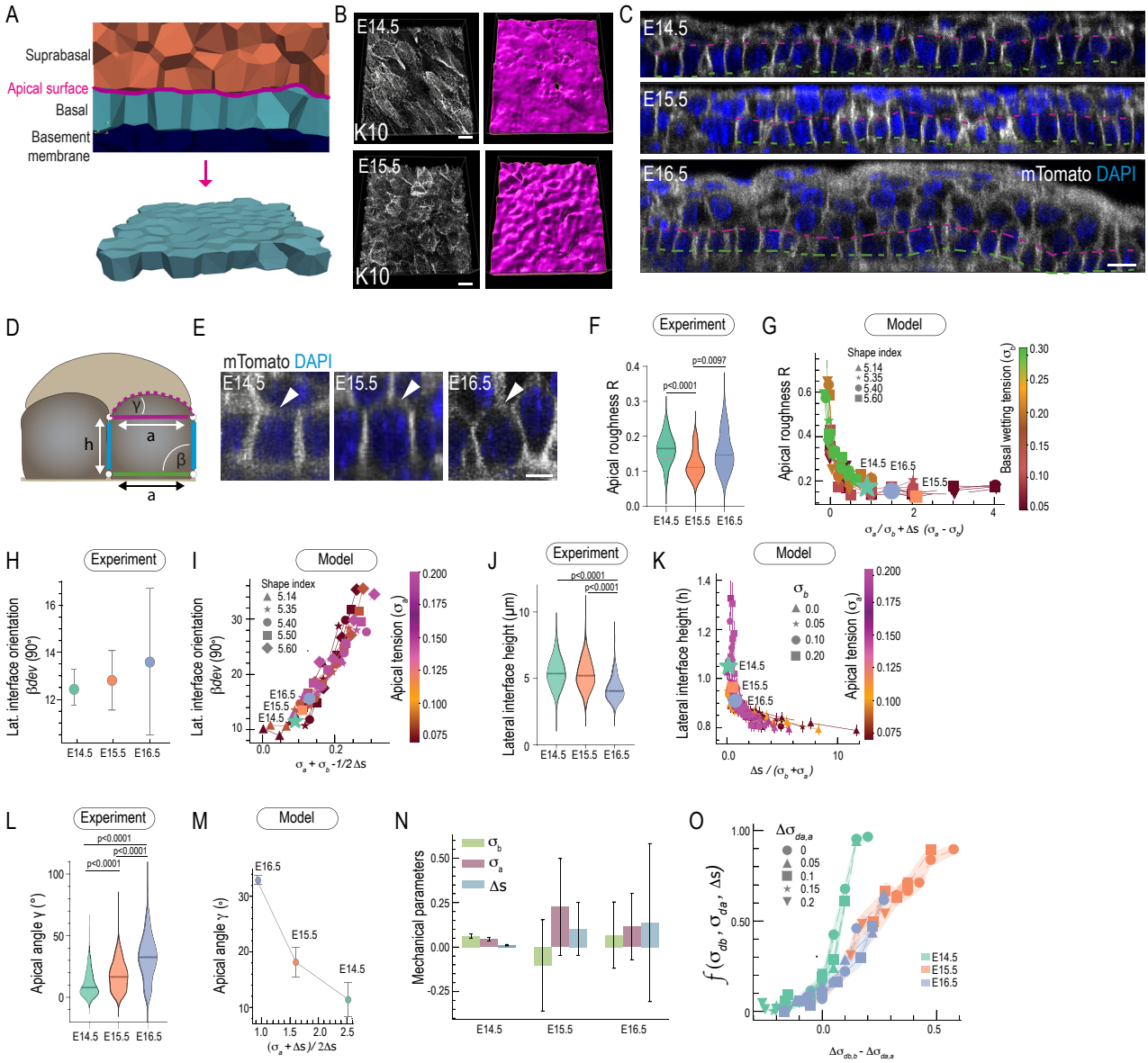


**Figure 3. A substantial mechanical energy barrier emerges at around E15.5 impacting delamination.**

**A.** Schematic representation of tissue-scale geometric parameter of surface roughness in the 3D vertex model. **B, C.** Representative experimental whole mount (B) and cross section images (C) of surface roughness measurements (scale bars 10 μm). **D.** Schematic representation of cell-scale geometric parameters. **E.** Representative image of tissue cross section across developmental stages for apical curvature angle (scale bars 5 μm). **F-K** Experimental observables (left panels) and corresponding collapsed simulation data (right panels) measured in the 3D model simulations across mechanical parameter space $(\sigma_a, \sigma_b, \Delta s)$. Corresponding averages of *in vivo* observables converted to simulation units specified as green, orange and blue symbols (experimental N>400 cells (J/K); >25 fields of view (L) >130 cells (I) timepoint pooled from n=3 mice; Kruskal-Wallis/Dunn's; n>85

simulations for each parameter set). **L, M.** Experimentally measured apical angles and corresponding simulation data as a function of vertex model parameters required by force balance (experimental N>400 cells; n>85 simulations for each parameter set). **N.** Best-fit vertex model parameters $\sigma_b$ (green), $\sigma_a$ (pink), $\Delta s$ (blue) to the cell and tissue geometry observed at each stage; error bars represent uncertainty in the fit (see Supplemental Methods). **O.** Simulation-predicted delamination rates when delaminating cells alter their mechanical properties from the background basal cells by $\Delta\sigma_{da,a}$ (apical) and $\Delta\sigma_{db,b}$ (basal). Rate is the fraction that delaminates in a fixed time window t = 2000 timesteps, corresponding to τ ~ 20 simulation time units (n>85 simulations per parameter set).

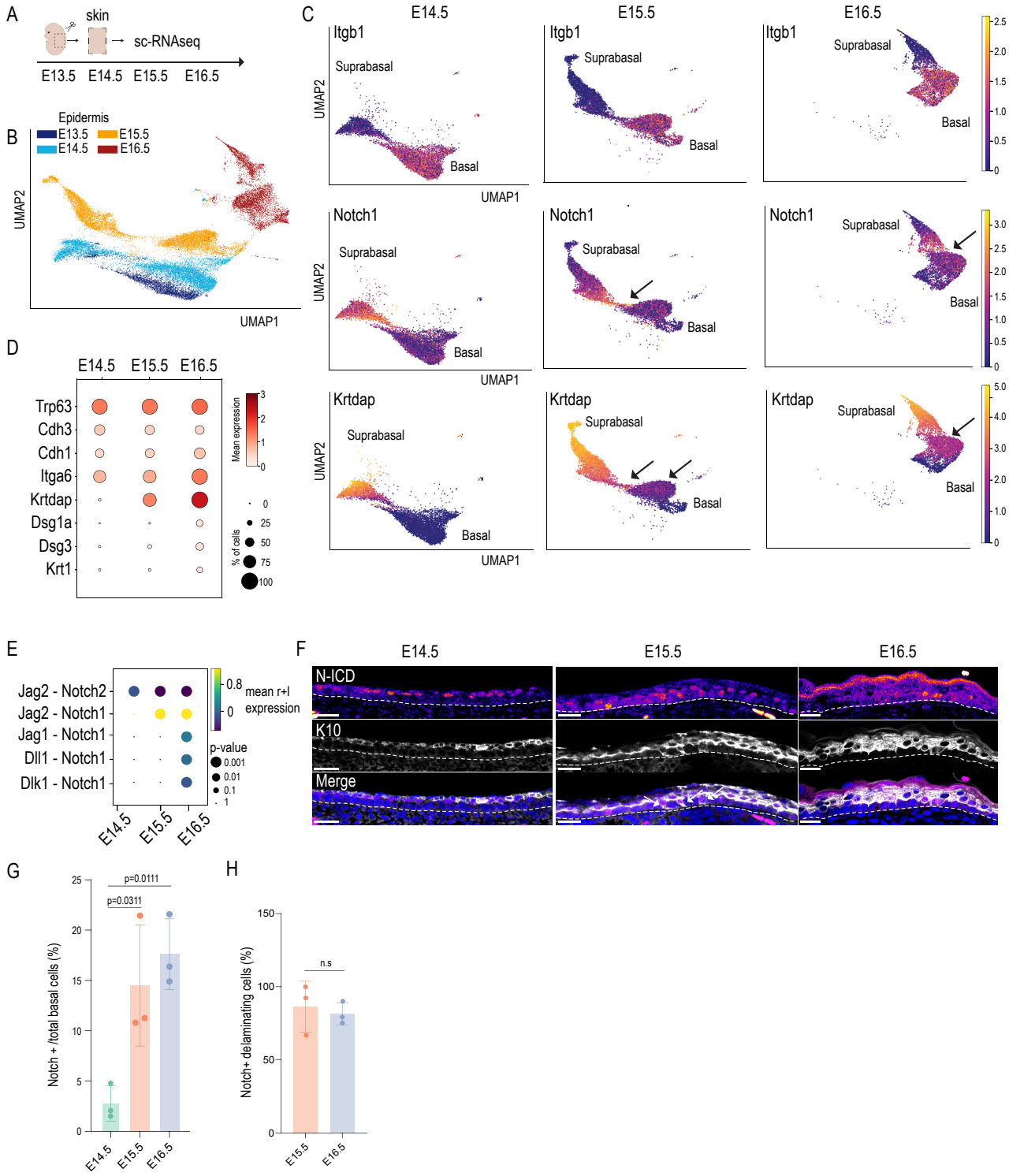


**Figure 4. A committed basal population characterized by Notch activation emerges at E15.5**

**A.** Schematics of the scRNAseq experiment. **B.** UMAP representation of the Leiden clusters of filtered epidermal cells from scRNAseq. Embryonic stages of cells are color coded. **C.** UMAP projections of basal identity and differentiation gene expression across E14.5-E16.5.

1119 Arrowheads mark transition population between basal and suprabasal cells. **D.** Dotplot of
1120 selected genes across E14.5-E16.5 basal cells. Note increased expression of differentiation
1121 genes in basal cells of E15.5 and E16.5 embryos. **E.** Dot plot of receptor-ligand (r+l) analyses
1122 between basal stem cells across E14.5-E16.5. Note increased predicted Jag2-Notch signaling
1123 interaction at E15.5 and E16.5. **F-H.** Representative images (F) and quantification (G, H) of
1124 tissue sections from E14.5- 16.5 embryos stained against Notch intracellular domain (N-ICD)
1125 and K10. Note emergence of N-ICD-K10- positive delaminating basal cells at 15.5. Dotted
1126 line marks basement membrane (mean ±SD; scale bars 20 µm; n=3 embryos/stage; Two-way
1127 ANOVA/Tukey's (G); Mann-Whitney (H)).

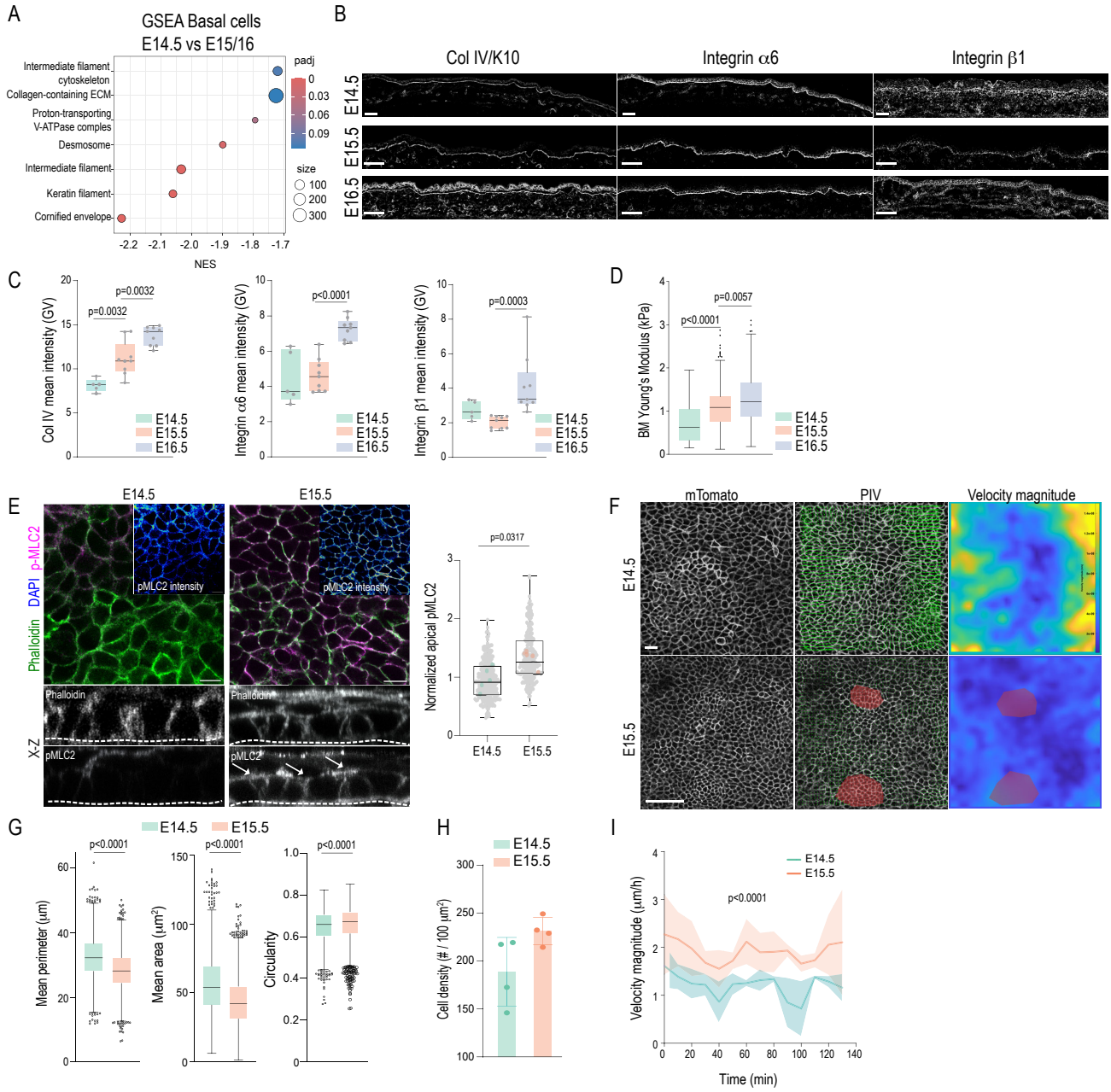


1128

1129 **Figure 5. Generation of the mechanical boundary at E15.5 is concomitant with**
1130 **stiffening of the basement membrane and rigidification of the basal layer**

1131 **A.** Dot plot of Gene set enrichment analyses (GSEA) from differentially expressed genes in
1132 basal cells of E14.5 versus E15.5/E16.5 embryos from scRNAseq data. **B, C.** Representative
1133 images (B) and quantification (C) of tissue sections from E14.5- 16.5 embryos analyzed by
1134 mass cytometry. Note increased expression of basement membrane Collagen IV
1135 (counterstained with K10) and integrins α6 and β1 (mean ±SD; scale bars 50 μm; n=3
1136 embryos/stage; Two-way ANOVA/Tukey's (Left and middle panel), Kruskal-Wallis/Dunn's
1137 (right panel)). **D.** Basement membrane Young's moduli extracted from AFM force
1138 indentation experiments (Tukey's box and whiskers; n>200 force curves pooled across
1139 3embryos/stage; Kolmogorov-Smirnov). **E.** Representative images and quantification of skin
1140 wholemounts from E14.5 and E15.5 embryos stained for pMLC2 and phalloidin. Note
1141 increased pMLC2 intensity at cell junctions and interface between basal and suprabasal
1142 layers (arrows) (min-max box and whiskers; scale bars 10 μm; n=5 embryos/stage; Mann-
1143 Whitney)**. F.** Representative snapshots from live imaging movies and subsequent PIV
1144 analyses of velocity magnitudes of E14.5 and E15.5 epidermis from membrane-Tomato
1145 (mTomato) reporter mice. Red masks mark excluded hair follicle areas (scale bars 50 μm).
1146 **G.** Quantification of 2D cell perimeter, area and circularity from data in (A) (Tukey's box
1147 and whiskers; n>2300 cells pooled across 3 embryos/stage; Mann-Whitney). **H.**
1148 Quantification of cell densities from data in (A) (mean ±SD; n=4 embryos/stage; Mann-
1149 Whitney). **I.** Quantification of velocity magnitudes from data in (A). Note attenuated velocity
1150 at E15.5 (mean ±SD; n=4 embryos/stage; Linear Mixed-Effects model.

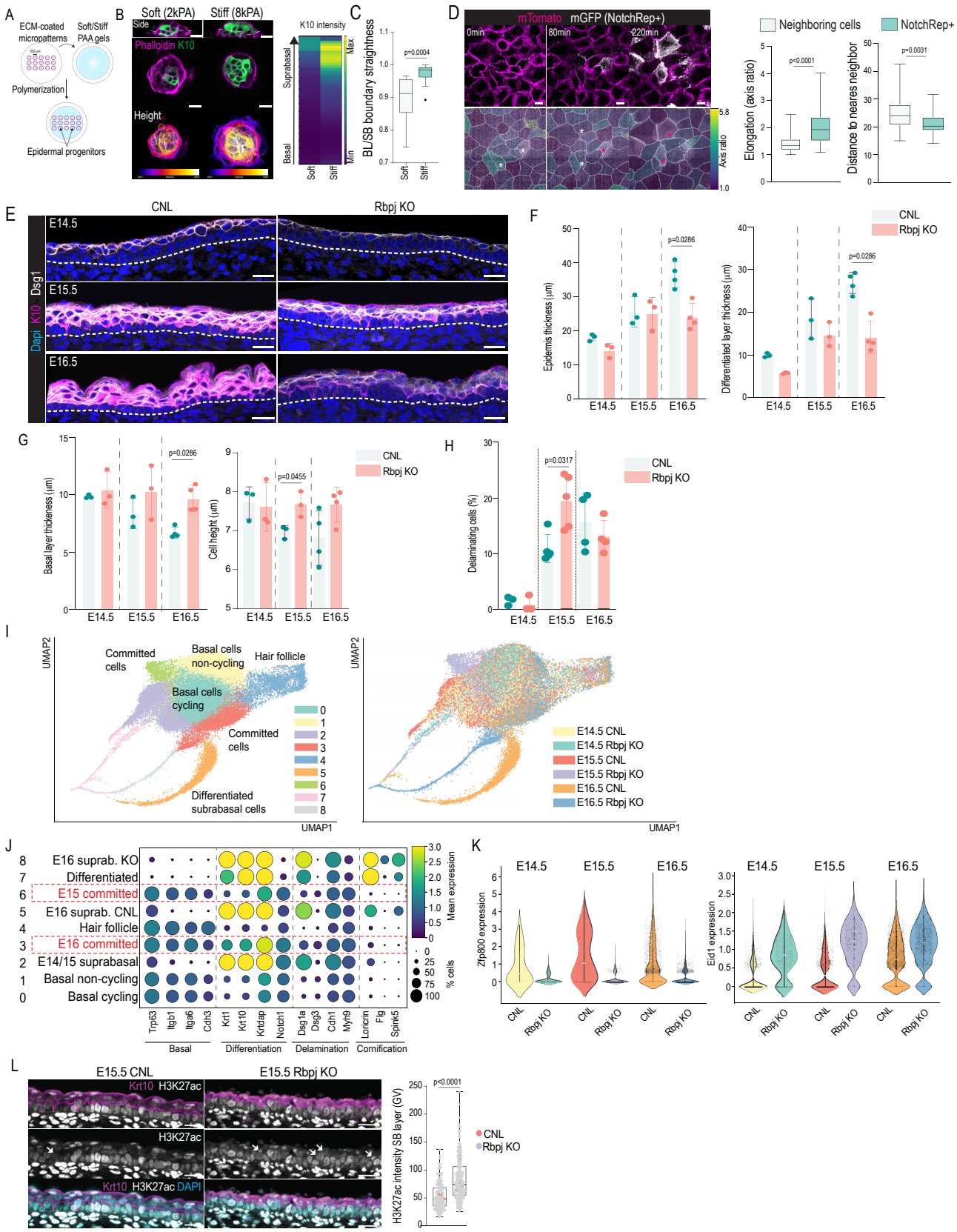


**Figure 6. Tissue rigidity and cell shape changes drive Notch- delamination and control of tissue crowding**

**A.** Schematic illustration of micropatterning of soft and stiff polyacrylamide (PAA) hydrogels. **B.** Representative images of primary epidermal progenitors stained with K10

1156 (green) and phalloidin (magenta) cultured on 100-µm-diameter micropatterns on 2.5 kPa
1157 (soft) or 8 kPa (stiff) PAA gels. K10 mean intensity was quantified as a function of the
1158 distance from the bottom of the micropatterns. Note the increased K10 mean intensity in the
1159 suprabasal region on stiff substrates. **C.** Quantification of boundary straightness between the
1160 basal layer (bottom) and the first suprabasal layer (upper layer). (Tukey's box and whiskers,
1161 n= 10 (soft); 15 (stiff) patterns pooled across 3 independent experiments; Mann-Whitney). **D.**
1162 Representative snapshots and quantification of live imaging movies from epidermal
1163 progenitor cell monolayers from mTomato/mGFP-Cre reporter mice crossed with Notch1-
1164 ICD-Cre to detect cells that activate Notch (mGFP+). Note increased elongation and local
1165 cell density of cells (white asterisk) that subsequently activate Notch signaling (red asterisk).
1166 Dotted circle marks delamination of Notch-Reporter-positive (NotchRep+) cell (min-max
1167 box and whiskers; n=38 Notch+ cells pooled across 3 independent experiments; Mann-
1168 Whitney; scale bars 10 µm). **E.** Representative images of tissue sections from E14.5-16.5
1169 embryos of control and Rbpj-KO mice stained against K10 (magenta) and Desmoglein 1
1170 (Dsg1; white) (images representative of >3 embryos/stage; scale bars 20 µm). **F.**
1171 Quantification of epidermal thickness from data in (A). Note reduced total and differentiated
1172 layer thickness of Rbpj-KO epidermis at E16.5 (mean ±SD; n=3 embryos/E14.5 and E15.5,
1173 4/E16.5; Mann-Whitney). **G.** Quantification of basal layer thickness and cell height from data
1174 in (E). Note increase basal layer thickness and cell height of Rbpj-KO epidermis emerging at
1175 E15.5 (mean ±SD; n=3 embryos/E14.5 and E15.5, 4/E16.5; Mann-Whitney). **H.**
1176 Quantification of delaminating cells from data in (E). Note increase in delaminating cells in
1177 Rbpj-KO epidermis at E15.5 (mean ±SD; n=3 (E14.5), 5 (E15.5), 4 (E16.5) embryos; Mann-
1178 Whitney). **I.** UMAP representation of the Leiden clusters (left panel) and biological samples
1179 (right panel) of filtered epidermal cells from scRNAseq. **J.** Dotplot of selected genes across
1180 E14.5-E16.5 epidermal cells. Clusters 3 and 6 (in red) represent committed basal cell
1181 populations enriched in Rbpj-KO cells of E15.5 and E16.5 embryos. **K.** Violin plots of
1182 Zfp800 of Eid1 expression across E14.5-E16.5 in control and Rbpj-KO epidermal cells. **L.**
1183 Representative images and H3K27ac nuclear intensity quantification from tissue sections
1184 from E15.5 embryos of control and Rbpj-KO mice stained for H3K27ac (grey), K10
1185 (magenta) and DAPI (cyan) (n= 176 (CNL), 234 (Rbpj-KO) cells pooled across 3 (CNL) /4
1186 (Rbpj-KO) embryos; Student's t-test; Scale bars 20 µm.)

1187

## Supplementary Figures

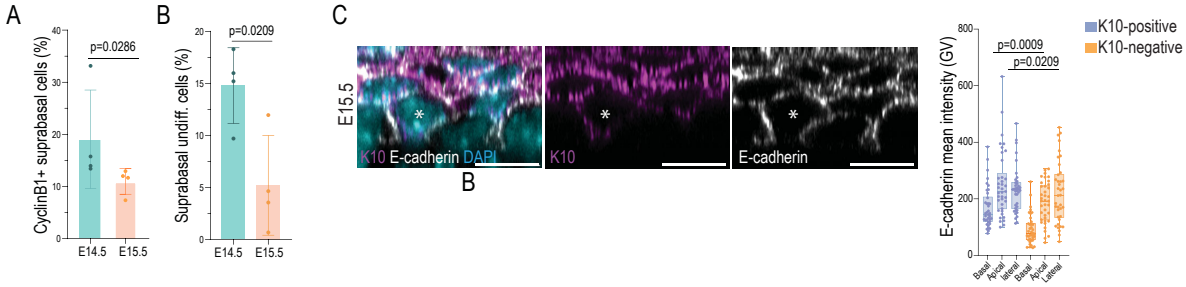


**Supplementary Figure 1.**

**A.** Quantification of differentiated (K10-positive) CyclinB1+ cells in the suprabasal layer (mean ±SD; n=4 embryos /stage; Mann-Whitney) **B.** Representative images and quantification of delaminating cells in E15.5 embryo from 3D whole mounts stained against E-cadherin, K10 and DAPI. Delaminating cell is marked with a white asterisk; scale bars 10 µm; min-max box and whiskers; n=38 cells pooled across 3 embryos; Friedman/Dunn's).

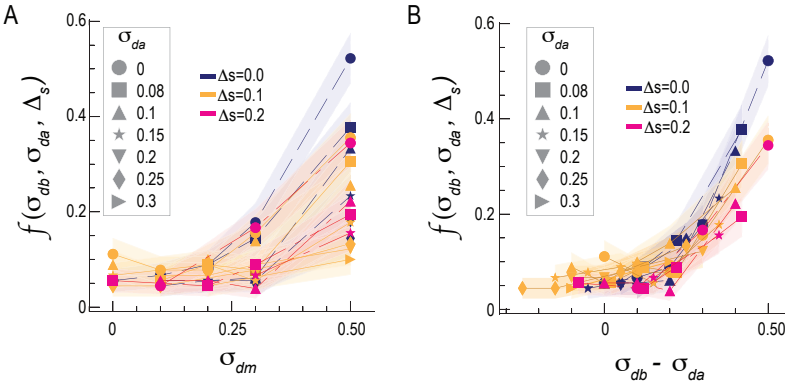


**Supplementary Figure 2. Systematic quantification of delamination rates as a function of the properties of the delaminating and stiffness of the surrounding tissue $\Delta s$**

**A.** Uncollapsed delamination rates. **B.** Delamination rates plotted as a function of $\sigma_{db} - \sigma_{da}$, which do not fully collapse, indicating that an additional energetic contribution is required. Figure 2D in the main text shows that adding the term $c\,\Delta s$leads to a collapse of the curves onto a single master curve as a function of $\sigma_{db} - \sigma_{da} + c\,\Delta s$.

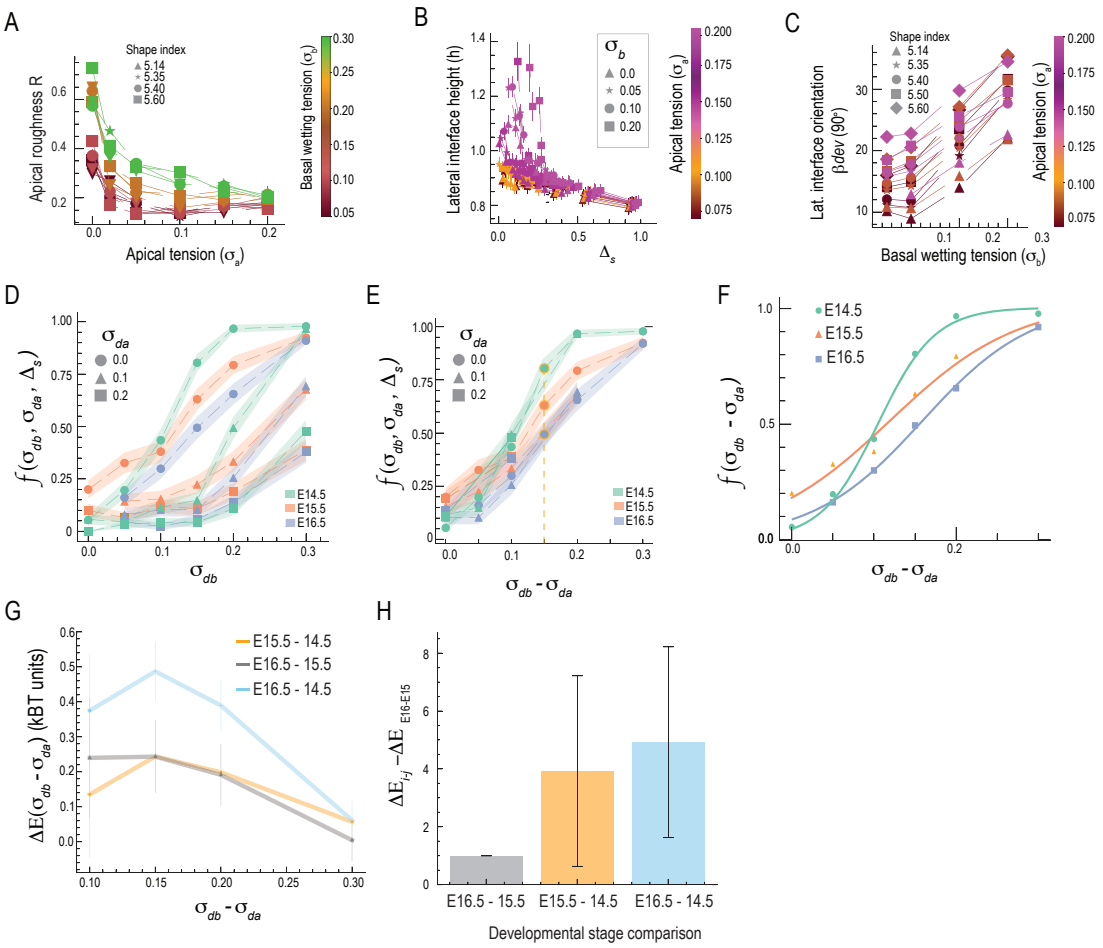


**Supplementary Figure 3. Geometric observables for mechanical barrier and quantification of delamination rates and associated energy barriers as function of delaminating cell properties.**

**A-C.** Uncollapsed plots of basal-suprabasal interface roughness, basal cell lateral interface height, and lateral interface orientation, respectively, measured in the 3D model simulations across mechanical parameter space ($\sigma_a, \sigma_b, \Delta s$). Corresponding collapsed plots are shown in main Fig. 3G, I, K. **D.** Quantification of delamination rates data as function of the delaminating cell tensions ($\sigma_{db}, \sigma_{da}$) parameter space. **E.** Data from (F) collapses as a function of $\sigma_{db} - \sigma_{da}$. **F.** Curve fits to the collapsed delamination rate data shown in panel (B) across the developmental stages. **G.** Quantification of the differences in energy barriers between developmental stages as a function of the differences in delaminating cell properties ($\sigma_{da}, \sigma_{db}$). **H.** Normalized averages (normalized by the energy barrier difference between stages E16 and E15) of the differences in energy barriers between stages E15.5 and E14.5, and between E16.5 and E14.5, plotted as a function of $\sigma_{db} - \sigma_{da}$.

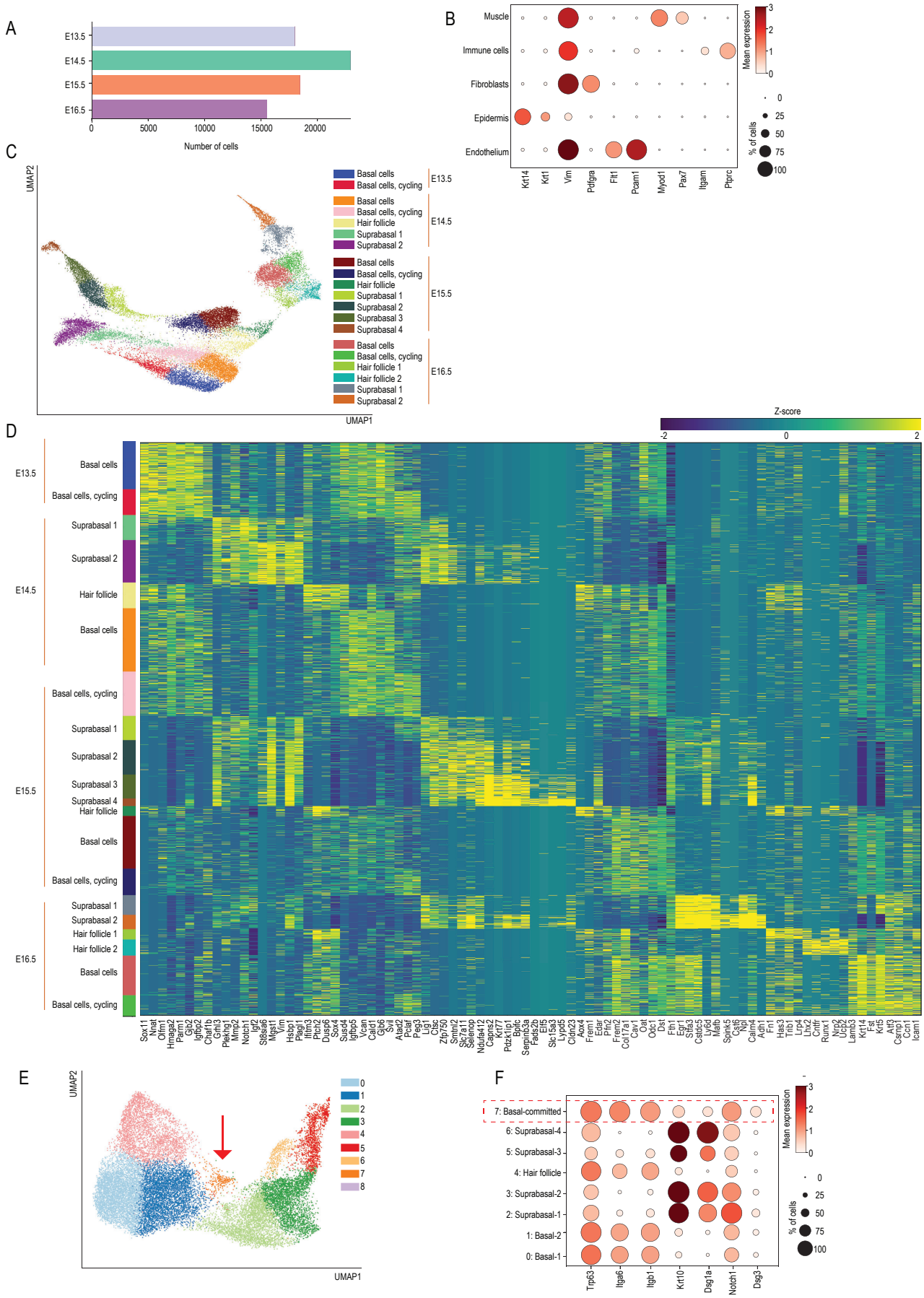


Supplementary Fig. 4

**Supplementary Figure 4.**

1220 **A.** Bar plot showing number of sequenced cells/genotype. **B.** Dot plot of selected key cell
1221 type-specific marker genes across annotated cell types. **C.** UMAP visualization of Leiden
1222 clusters of epidermal cells with main cell states annotated. **D.** Heatmap of marker genes for
1223 epidermal Leiden clusters. **E.** UMAP visualization of Harmony integrated epidermal cells.
1224 Red arrow indicates committed cell population. **F.** Dot plot of selected key cell type-specific
1225 marker genes across annotated cell types from Harmony integrated epidermal cells. Red
1226 dotted rectangle indicates committed cell population.

1227 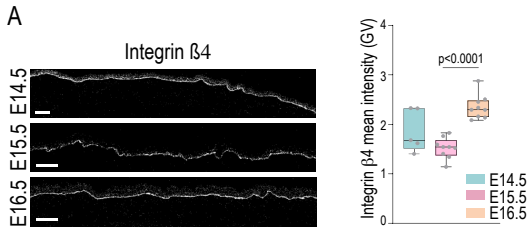


1228 **Supplementary Figure 5.**

1229 **A.** Representative images and quantifications of tissue sections from E14.5- 16.5 embryos
1230 analyzed by mass cytometry. Note increased expression of integrin β4 (mean ±SD; scale bars
1231 50 µm; n=3 embryos/stage; Two-way ANOVA/Tukey's.

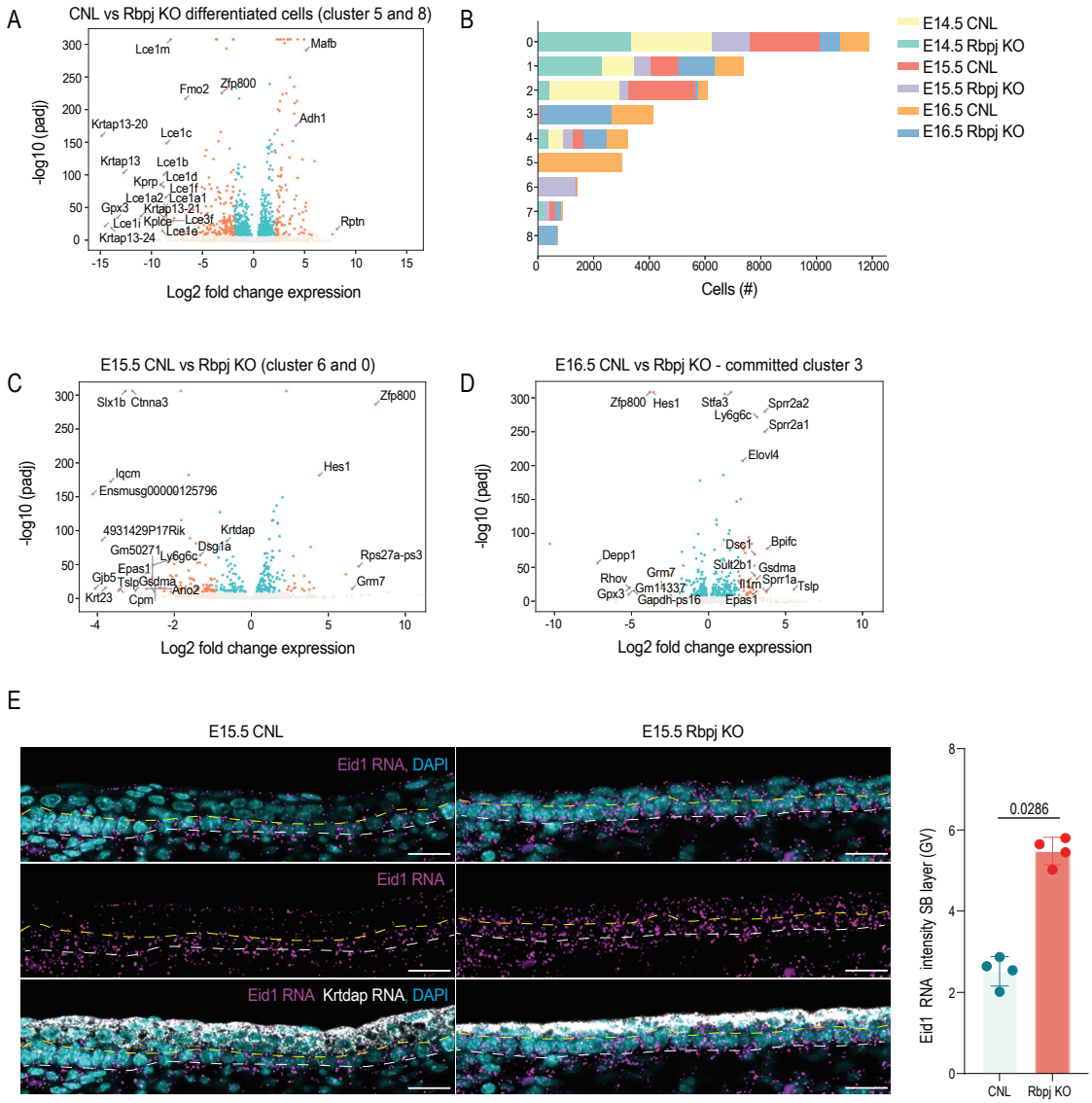


**Supplementary Figure 6.**

**A.** Volcano plot showing differentially expressed genes between Rbpj-KO and CNL epidermis from differentiated cell clusters 5 and 8. **B.** Bar plot showing number of sequenced cells/embryonic stage and genotype across Leiden clusters. **C.** Volcano plot showing differentially expressed genes between E15.5 Rbpj-KO and CNL epidermis from clusters 6 and 0. **D.** Volcano plot showing differentially expressed genes between E16.5 Rbpj-KO and CNL epidermis from cluster 3. **E.** Representative images and quantification of tissue sections from E15.5 embryos of control and Rbpj-KO mice of the expression of Eid1 (magenta) and Keratin-dap (grey) detected by RNA in situ hybridization. Dotted lines mark basal layer (n=4 embryos/condition; Mann-Whitney). Scale bars 20 µm.